Local Brain Temperature Manipulation System and Physiological Parameters (R2', CBF and ADC) Measurements in Acute Stroke

Qingwei Liu

A thesis submitted to the faculty of the University of North Carolina at Chapel Hill in partial fulfillment of the requirements for the degree of Master of Science in the Department of Biomedical Engineering.

Chapel Hill

2010

Approved by:

Dr. Weili Lin

Dr. Hongyu An

Dr. Dinggang Shen

ABSTRACT

Qingwei Liu: Local Brain Temperature Manipulation System and Physiological Parameters (R2', CBF and ADC) Measurements in Acute Stroke
(Under the direction of Weili Lin)

Accurate prediction of final lesion is critically important for clinical decision making in the management of acute ischemia stroke patients. In addition to the widely utilized perfusion and diffusion parameters, an MR derived cerebral oxygen metabolism index OMI_ R2′, may be a potential candidate for infarction prediction. In this study, we evaluated how these MR parameters may delineate infarction in rats with ischemic injury.

There is overwhelming evidence from animal studies showing that cooling may improve outcome after cerebral ischemia. However, how physiology parameters during ischemic injury are modulated by brain temperature is largely unknown. In this study, we designed an MR compatible focal brain temperature manipulation system, which can regulate brain temperature accurately. The relationship between T1 and temperature in brain tissue was investigated, which can be used to derive the brain temperature under hypothermic conditions. The relationship between CBF and temperature was also studied under ischemic condition.

To my wife, Jin Shi

TABLE OF CONTENTS

LIST OF TABLES

Table

LIST OF FIGURES

Figure

ABBREVIATIONS

aCBV	Cerebral arterial blood volume
ADC	Apparent diffusion coefficient
BOLD	Blood oxygenation level dependent
CBF	Cerebral blood flow
CBV	Cerebral blood volume
CMRO2	Cerebral metabolic rate of oxygenation
CPMG	Carr-Purcell-Meiboom-Gill
DWI	Diffusion weighted imaging
emf	Electromotive force
EPI	Echo planar imaging
FLASH	Fast low angle shot imaging
Gd-DPTA	Gadolinium diethylenetriamine pentaacetic acid
Hct	Hematocrit
MRI	Magnetic resonance imaging
MTT	Mean transit time
OEF	Oxygen extraction fraction
PET	Positron emission tomography
PWI	Perfusion weighted imaging
ROI	Region of interest
SNR	Signal-to-noise
SVD	Singular value decomposition
tPA	Tissue plasminogen activator
vCBV	Cerebral venous blood volume

CHAPTER 1

INTRODUCTION

Magnetic Resonance Imaging (MRI) has become a widely used and powerful imaging modality because of its flexibility, sensitivity to broad range of tissue properties and noninvasive nature. Due to the complexity of signal formation, MRI provides not only anatomic information, but also information of brain function and other biological homodynamic processes, such as Cerebral Blood Flow (CBF)[1], Cerebral Blood Volume (CBV), etc. With MRI, a better understanding of the relationships among brain structure, function, and pathology is feasible.

1.1 Backgrounds

Stroke is a global health problem affecting approximately 750,000 people annually in the United States alone and ranks as the third leading cause of death and the most common cause of disability in most developed countries. Based on the underlying causes, strokes can be classified into two major categories: ischemic and hemorrhagic stroke. Ischemia is due to interruption of the blood supply to part of the brain tissue, leading to dysfunction and necrosis of the brain tissue in that area, while hemorrhage is due to rupture of a blood vessel or an abnormal vascular structure. About 87% of strokes are due to ischemia and the rest are due to hemorrhage.

Until now, intravenous administration of Tissue Plasminogen Activator (tPA), which is used to dissolve the clot and unblock the artery, is the only FDA approved therapy for the treatment of acute ischemic stroke patients. In the National Institute of Neurological Disorders and Stroke trial (NINDS)[2], patients treated with t-PA were at least 30 percent more likely to

have minimal or no disability at three months on the assessment scales as compared with patients received placebo. Symptomatic intracerebral hemorrhage within 36 hours after the onset of stroke occurred in 6.4 percent of patients given t-PA but 0.6 percent of patients given placebo ($P < 0.001$). The mortality rate in cases of symptomatic ICH was 47% but the global mortality rate was lower in the tPA group than in the placebo group (17% vs. 21%) because of a reduction in death not related to hemorrhage. The pooled analysis of four large placebo controlled trials (NINDS, ECASS, ECASSII, ATLANTIS) involving 3000 patients showed intravenous tPA (when given within the 3 hour window) resulted in improved clinical outcomes with a relative risk reduction of about 9.8% for achieving minimal or no disability at 3 months.[3-5] Although the control studies show that intravenous tPA is effective and safe when given under restrictive conditions within 3 hours after stroke onset, the data for a longer therapeutic window, between 3 and 6 hours remain controversial. The expected functional improvement and the risk of intracranial hemorrhage greatly depend on selective clinical and imaging criteria[6]. It is recommended by the American Heart Association and the American Academy of Neurology that tPA should be administrated for acute ischemic stroke within 3 hours of onset of symptoms[2] while there are no other contraindications (such as abnormal lab values, high blood pressure, or recent surgery). Recently the Third European Cooperative Acute Stroke Study (ECASS-3) demonstrated a benefit of treatment for acute stroke even until 4.5 hours after onset of occlusion.[7] Since thrombolysis is not beneficial for all stroke patients, strict criteria should be applied before treatment. As time from symptom onset increases, the need for careful patient selection also increases.

Since the therapeutic window for tPA is short, only a small percent of patients are eligible for treatment. To alleviate this problem, two potential approaches have been proposed 1) identifying the sub-group of patients who may benefit from tPA injection beyond 3 hours therapeutic window; and 2) utilizing a neuroprotective method to prolong the survive window of neurons under ischemic condition.

For the former approach, MR perfusion-diffusion mismatch has been a popular method in clinic to predict the salvable area in the brain. Although promising results have been shown, the validity of this approach is still under extensive scrutiny [8-13]. It was found that the diffusion lesion can reverse after reperfusion, while perfusion deficit cannot differentiate benign oligemia from penumbra. In contrast, it has been demonstrated that measures of cerebral metabolic rate of oxygen utilization may provide more accurate insights into tissue viability [14-17].

For the second approach, hypothermia is a potential candidate to extend the therapeutic window. The neuroprotective properties of mild hypothermia have been demonstrated in numerous experimental animal models[18, 19] and human studies[20], with significant improvement of ischemic stroke outcome. Hypothermia is more efficient than other methods because it can affect a wide range of cell death mechanisms simultaneously. Although hypothermia therapy is promising, there is no conclusion yet on the optimal duration, depth and the time of onset of hypothermia for ischemic stroke. Since different conditions may lead to very different results, it is imperative to address how hypothermia extends the therapeutic window. In this study, we focused on how brain tissue viability is modulated by brain temperature.

The following relevant background information to this study is provided.

1.1.1 Viable Tissue or Irreversible Damage

Ischemia is caused by a shortage of blood supply to an organ. Tissue is deprived of oxygen and other nutrition under ischemia. Based on the severity of ischemia and the elapsed time after ischemic onset, tissue can be potentially classified into ischemic core, penumbra and oligemia. Ischemic core, often referred to as irreversible ischemic injury, loses not only its electrical functions but also structural integrity. It will die regardless of any treatment. Ischemic penumbra, defined as a region exhibiting impaired electrical activity, but preserved morphologic integrity, cellular metabolism and viability [21-25]. Ischemic penumbra may be

salvaged by an effective treatment. The presence of penumbra is an evolving process depending on both the ischemic severity and the elapsed time since ischemic onset [26-29]. Several studies have demonstrated that salvageable tissue may still exist even beyond the 3 hours time window [27, 30-32]. Therefore, a means to delineate irreversible and reversible cerebral ischemic injuries may aid to select patients who may benefit from the tPA treatment even beyond the currently approved 3 hour window. Oligemia is the region with mild flow deficit and it can survive even without any treatment.

The mismatch between MR diffusion and perfusion images has been suggested to provide an estimate of the ischemic penumbra and is used in clinic within the first 6 hour after stroke onset to select patients who might benefit from thrombolysis.[33] Although promising results have been shown, this approach has been thought to be overly simplified and the validity of this approach is still under studied [8-13]. Recent findings indicate that the subtraction of the ischemic lesion on diffusion-weighted imaging (DWI) from the abnormality on perfusion-weighted imaging (PWI) is only a weak approximation of the penumbra.[8] The DWI defined ischemic core region often overestimates the final infarction volume, since it was found that the diffusion lesion can be recovered after reperfusion[34]. We have observed similar results in our study, with DWI lesion larger than the final lesion defined using T2 weighted images, especially with a short period of occlusion time, e.g. 45 minutes. In addition, the MR perfusion deficit is not reliable either since it cannot differentiate benign oligemia from the penumbra[8], thus making that the mismatch overestimates the penumbra.

In contrast, it has been demonstrated that measures of cerebral metabolic rate of oxygen utilization may provide more accurate insights into tissue viability [14-17]. During the process of cerebral oxygen metabolism, paramagnetic deoxyhemoglobins (deoxy-Hb) are present in capillaries and veins. The concentration of deoxy-Hb thus reflects oxygen extraction fraction (OEF) . Therefore, the measurements of $R2'$, which is proportional to the concentration of deoxy-Hb, could potentially be used to indirectly estimate OEF. To evaluate whether $R2'$ may provide additional information concerning the metabolic state of ischemic tissue, Geisler et al

examined R2′ in regions with abnormal apparent diffusion coefficient (ADC). They observed an elevated R2′ in the ischemic hemisphere when compared to the unaffected hemisphere. Moreover, the increase of R2′ is highest in ADC lesion, followed by the lesion growth and surviving regions. Their observation suggested that an increase of R2′ may correspond to an increase of OEF in ischemia. More recently, Siemonsen et al have reported that R2′ > ADC mismatch is a more specific predictor of infarct growth than is TTP >ADC mismatch in thrombolytic treated patients. These findings are encouraging and may reveal the clinical utility of R2′ in acute stroke. Similar to the PET measured OEF, R2′ only reflects the oxygen metabolic demand. It has been suggested in the PET literature that cerebral metabolic rate of oxygen (CMRO2), which reflects the balance between oxygen delivery (CBF) and demand (OEF), may be a more specific marker for tissue viability. Although quantitative measures of CMRO2 can be derived using PET, an MR based approach, if proven to be capable of providing similar information on oxygen metabolism, may greatly facilitate routine clinical application. In line with the findings in PET literature, an MR derived cerebral oxygen metabolism index, which is a product of CBF and R2′ (OMI_ R2′), might be able to separate penumbra from irreversible core.

1.1.2 Neuroprotective Effects of Hypothermia

Hypothermia has been proved to improve the outcome of acute cerebral ischemia in laboratory animals[18, 19]. In humans, hypothermia is an established tool for the protection of brain tissue during surgery and it seems to improve the outcome of patients, who have suffered an acute ischemic stroke [20]. At normal temperature, brain tissue at risk cannot survive when the metabolic variables decline below a specific threshold [5–7]. The duration of this decline is often referred to as the critical time window of therapeutics. For ischemic stroke, the critical time-window of 3 hours is too narrow for most of the stroke patients to receive tPA. One alternative may be to combine tPA with hypothermia so as to extending the therapeutic window of tPA [7–9]. Thus, both the time of initiating the cooling and the

subsequent duration of hypothermia play important roles in determining the efficacy of this treatment.

Pre-clinical studies have suggested that hypothermia affects a wide range of cell death mechanisms including reduction of the cerebral oxygenation and energy metabolic activities [35-39], alteration in oxygen free radicals release [40-44], decreases in the release of excitotoxic neurotransmitters [45-47], reduction or delay in apoptosis [48-50], and preservation of the blood-brain barrier [51-54]. The potential of hypothermia has recently been underlined by randomized clinical trials in patients with global cerebral ischemia after cardiac arrest[55] and in infants with moderate or severe hypoxic-ischemic encephalopathy [56], in which cooling reduced mortality and disability. In addition, several prospective observational studies have demonstrated that higher body temperatures are associated with poor outcome after stroke[20, 57]. In animal focal ischemia models, hypothermia reduces infarct size by 44% [95% confidence interval (CI), 40-47%][58], with the highest efficacy obtained with cooling to a lower temperature (<=31 °C). The effect of cooling was most robust when started before or at the start of vessel occlusion, but there was no clear time-dependency thereafter. The efficacy was higher in transient than in permanent occlusion models, but the effect in the latter was still substantial (37%; 95% CI). In addition, hypothermia significantly improves the survival rate, which is in accordance with data from the MCA occlusion model even for delayed application and reperfusion[54]. Although hypothermia therapy is promising, there is no conclusion yet on the optimal duration, depth of cooling and the time of onset of hypothermia. Thus, a more thorough investigation of the mechanisms of how hypothermia benefits the ischemic stroke may provide theoretical basis to extend the therapeutic window.

At present, systemic surface cooling is the most widely used method to induce and maintain mild hypothermia. Although these methods are effective, the decreased body temperature can lead to multiple side effects, such as pneumonia, arterial hypotension, thrombocytopenia, bradycardia, infection and myocardial infarctions, [59-63]. Instead, selective brain cooling methods can induce hypothermia in the brain locally, while

maintaining the body temperature within the normal range, which could suppress the side effects. In this study, we designed an MR compatible local brain temperature manipulation system, which is able to regulate brain temperature consistently and accurately for a desired period of time, while keeping the body temperature within normal range. Using this local brain cooling device, we studied the relationship between cerebral perfusion and brain temperature in ischemic stroke as well.

1.1.3 Brain Temperature Mapping

It has been suggested that the brain is sensitive to temperature alterations [64-66]. A small decrease in brain temperature by only a few degrees leads to significant neuro-protective effects in ischemic stroke, while a slightly increased brain temperature exacerbates brain injury[19, 48, 51, 64, 66-77]. In order to evaluate how temperature alters brain metabolism, an accurate measurement of brain temperature is important. A direct measurement of brain temperature with a temperature probe is invasive and cannot provide spatially resolved information. In recent global cerebral ischemia and head injury rodent studies, the temperature in temporal muscle was measured to represent the brain temperature. However, it has been reported that the temperature in temporal muscle is different from the brain temperature. There are also studies reporting that the temperature in temporal muscle was markedly lower than brain in rats during ischemic condition with the MCAO model.

In addition, with the local surface cooling method, where there is a large temperature gradient inside the brain, it is not possible for a single temperature probe to reflect the spatial temperature information. Therefore, a pixel-by-pixel brain temperature map is desirable to reliably reveal the potential relation between brain temperature and other physiological parameters.

1.2 Accomplishment

The accomplishments in this study are listed as below.

1. We developed an MR compatible device which can manipulate local brain temperature accurately and maintain for a desired period of time, while preserving a normal systemic body temperature and other physiology parameters.

2. The relationship between T1 and temperature in the brain was derived.

3. The relationship between CBF and temperature was derived at different severity of ischemic stroke regions.

4. A GESSE sequence was applied to measure R2', with a multi-navigator echo method for motion correction and the Z-shimming method for B0 field inhomogeneity correction.

5. The relationship between different MR parameters (ADC, CBF, R2' and OMI_R2) in rats with a short duration of ischemic injury (45 minutes MCAO) was studied.

CHAPTER 2

MR COMPATIBLE LOCAL COOLING DEVICE DESIGN AND STUDY OF RELATIONSHIP BETWEEN CEREBRAL BLOOD FLOW AND T1 WITH TEMPERATURE

2.1 Theory: Relevant MR Principals and Instrumentation Concepts

The purpose of this chapter is to introduce the relevant MR principles related to the study, and instrument design concepts.

2.1.1 Magnetization, Relaxation and the Bloch Equation

2.1.1.1 MR Signal Formation

MRI is based on the interaction between proton spin and the external magnetic field, B0. The dominant nucleus in MRI is the proton in hydrogen. Its interaction with the external field results in the precession of the proton spin about the field direction. The procession angular frequency for the proton magnetic moment vector is given by

$$\omega_0 = -\gamma.\vec{B}_0 \qquad (2.1)$$

where ω_0 is the Lamar Frequency, B0 is the main (external) magnetic field strength in Tesla, γ is the gyromagnetic ratio, a constant equals to 2.675x10e8 rad/T/sec for proton.

In order to generate a detectable signal by the receiving coil, the magnetization vector must be tipped away from the external field direction. The magnetic field produced by the

proton spins yields a changing magnetization flux in the nearby coil. According to the Faraday's law, the electromotive force (emf) would be induced by the change of magnetization flux.

$$emf = -\oint \frac{d}{dt}(\vec{M}.\vec{B}_{rf})d^3r \qquad (2.2)$$

Then, the induced emf is amplified and transferred into signal and eventually be reconstructed into an image.

2.1.1.2 T2, T1, T2' Relaxation, B0 Inhomogeneity and Bloch Equation

In an idealized system, all protons have the same precession frequency $\omega = \gamma B_0$. However, the B0 field is never uniform in real system, which leads to a distribution of resonance frequencies. Over time, this distribution can lead to a dispersion of magnetic spin vectors, which induce the loss of signal.

Based on the scale relative to voxel size, the B0 field inhomogeneity can be divided into three scales, the microscopic, mesoscopic and macroscopic levels.

The microscopic inhomogeneities, with a size at the proton diffusion distance level, induce irreversible signal decay, which is represented by T2 relaxation. Spins experience local fields which are the combinations of the applied field and the fields of their neighbors. The local microscopic field inhomogeneities cause the spins to fan out in time leading to a reduction of net magnetization, called 'dephasing'. Several physical factors can cause the reduction of transverse magnetization. For instance, motion of molecules whose electrons produce local fields varies as a function of time.

The macroscopic inhomogeneity, with a size similar or larger than image voxel size, contributes to the reversible relaxation (T2' relaxation). Macroscopic field inhomogeneities usually come from magnet imperfections, such as body-air interfaces, large sinuses inside the body, etc. These B0 inhomogeneities are mostly undesirable because they generally provide no useful information of physiologic or anatomic interest. Rather, they lead to signal loss in

gradient-echo (GE) imaging, and image spatial distortions in both GRE and spin-echo (SE) imaging. The dephasing effect of macroscopic B0 inhomogeneities are time independent and the signal loss can be reverted by a 180-degree RF pulse in a SE sequence.

The mesoscopic inhomogeneity, with a size between the previous two scales, is also reversible and contributes to T2' relaxation. The blood vessel network in brain tissue creates mesoscopic field inhomogeneities that are tissue specific and are responsible for the Blood Oxygenation Level Dependent (BOLD) contrast. It is well known that as the oxygen content in blood changes, the local susceptibility in the blood also changes. The reason is because the deoxyghemoglobin in the blood vessels is paramagnetic and it affects the R2' relaxation constant. Thus the R2' value can be used to reflect the concentration level of deoxyhemoglobin in blood vessels, and further reflect the oxygenation in the blood.

The combined transverse relaxation time constant is represented by T2*, which is generally given as:

$$\frac{1}{T_2^*} = \frac{1}{T_2} + \frac{1}{T_2'} \tag{2.3}$$

For most magnetic resonance experiments, these "relaxations" dominate the signal decay. T1 relaxation is due to the interactions of the spins with their surroundings. After the magnetization has been rotated into the transverse plane, it will tend to grow back to along the direction of the static field B0. The rate of the regrowth can be characterized by a time constant T1, which is also called 'spin-lattice' relaxation time.

The Bloch equation is used to describe the interaction of a nuclear spin with an external magnetic field and its local environment when T1 and T2 relaxation are considered.

$$\frac{d\vec{M}}{dt} = \gamma\vec{M} \times \vec{B}_{ext} + \frac{1}{T_1}(M_0 - M_z)\hat{z} - \frac{1}{T_2}\vec{M}_\perp \tag{2.4}$$

The solutions are given as,

$$M_x(t) = e^{-t/T_2}(M_x(0)cos\omega_0 t + M_y(0)sin\omega_0 t) \tag{2.5}$$

$$M_y(t) = e^{-t/T_2}(M_y(0)cos\omega_0 t - M_x(0)sin\omega_0 t) \tag{2.6}$$

$$M_z(t) = M_z(0)e^{-t/T_2} + M_0(1 - e^{-t/T_1}) \tag{2.7}$$

From the solutions we can see, the transverse component of magnetization $\overline{M}$ is rotating in the x-y plane with a decay time constant T2, where rotation frequency ω_0 is the Larmor frequency. At the same time, its longitudinal component returns back to initial Magnetization M_0 with the relaxation time constant T1.

2.1.1.3 TOMROP Method for Measurement of T1

There are several ways to measure T1 relaxation time. The fast T One by Multiple Read Out Pulses (TOMROP) sequence[78] was utilized in our study. Here is a simple description of this method.

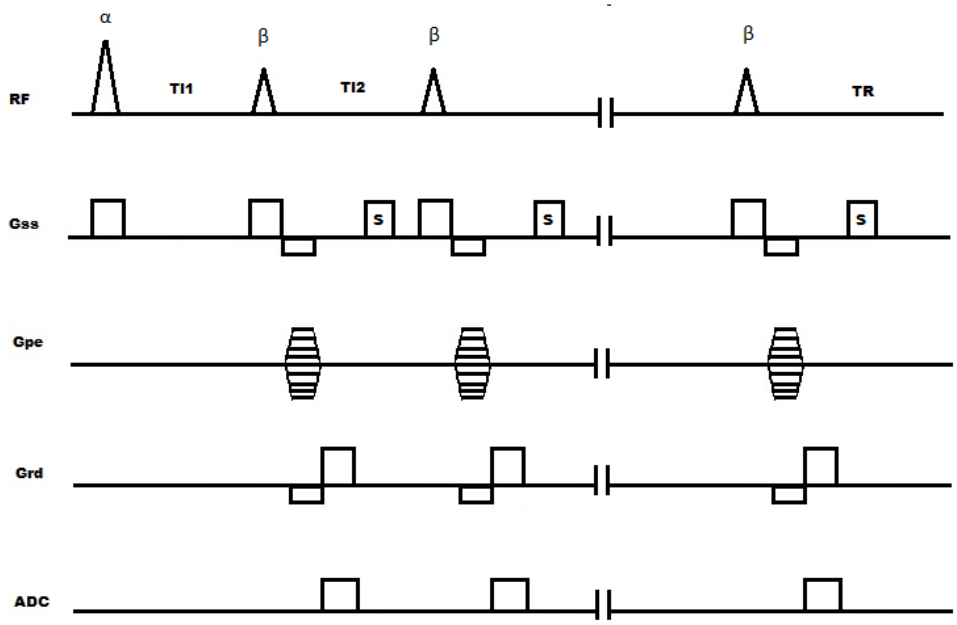

Figure 1. Diagram of Look-locker sequence for measurements of T1

As shown in figure 1, a selective RF pulse with a flip angle α (usually 180 degree) sets the longitudinal magnetization M_0 to the negative direction; then a series of interrogation pulses with a small flip angle β is applied to create a set of gradient echoes. The time between interrogating pulses as well as interrogating precession angles are chosen to be a constant. After acquisition of each gradient echo, the remaining transversal magnetization is destroyed by a spoiler gradient. The signal acquired at the nth echo can be derived as below,

$$S_n(i,j) = \left| s_\beta(i,j) M_n(i,j) \exp\left[-T_D / T_2^*(i,j)\right] \right| \quad (2.8a)$$

$$M_n = M_{eq}\left[F + \left(c_\beta E_2\right)^{n-1}(Q - F)\right] \quad (2.8b)$$

$$Q = \frac{F c_\alpha c_\beta E_r E_1 \left[1-\left(c_\beta E_2\right)^{N-1}\right]}{1 - c_\alpha c_\beta E_r E_1 (c_\beta E_2)^{N-1}} + \frac{c_\alpha E_1 (1-E_r) - E_1 + 1}{1 - c_\alpha c_\beta E_r E_1 (c_\beta E_2)^{N-1}} \quad (2.8c)$$

$$E_1 = \exp\left(-\frac{TI_1}{T_1}\right) \quad (2.8d)$$

where T2* is the characteristic decay constant of the FID and T_D is the time between the interrogation pulse and data acquisition, $E_r = \exp(-t_r / T_1)$ $E_2 = \exp(-TI_2 / T_1)$ and $c_\alpha = \cos(\alpha)$. TI is the time between α and β RF pulses. M_n is the longitudinal magnetization right after the nth RF pulse, and s_β is a constant depending on the small RF flip angle β. By fitting the experimental data set using equation (2.8), the T_1 value can be derived.

2.1.2 Relationship Between T1 and Temperature

Spin-lattice relaxation time (T1) has been demonstrated to be linearly proportional to temperature when it is below 45 ℃ [79-81]. This linear temperature dependence relationship of T1 with temperature T can be expressed as

$$T1 = T1_{ref} + m(T - T_{ref}) \quad (2.9)$$

where m is the coefficient constant, T_{ref} and T are the reference temperature (37℃) and current temperature, respectively. $T1_{ref}$ is the T1 value at the reference temperature.

2.1.3 Cerebral Blood Flow (CBF)

Tissue function depends heavily on perfusion, a process that brings nutritive blood supply and oxygen to the tissue through the arterial supply. There are at least two MRI methods can provide the measures of CBF, Dynamic Susceptibility Contrast (DSC) method and Arterial Spin Labeling (ASL) method. The advantage of ASL is that it uses endogenous labeled water proton as the contrast agent, while the DSC method uses exogenous paramagnetic contrast

agent instead. The ASL method is non-invasive and can be used to measure CBF repeatedly. In the first part of this study, the Continuous ASL (CASL) method was used to measure the blood flow, while DSC method was employed in the second part of the study.

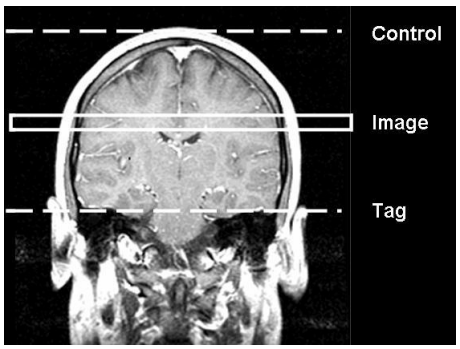

Figure 2. Continuous arterial spin labeling for measurement of CBF

An MR image can be used to measure the inflow of blood spins if those spins are in a different magnetic state compared to the static tissue. For the CASL method, the water proton was magnetically inverted (tagged, labeled) with a long RF pulse before entering the imaging slice of interest, as shown in the figure 2. The labeled arterial spins mix with the stationary spins in the imaging slice, reducing the signal intensity. Compared to the label procedure, a control image was acquired with the same RF pulse applied on a plane on the opposite side of imaging plane with the same distance. The difference between the labeled and control images can be used to evaluate blood flow. The derivation of CBF from the CASL is shown by Calamante et al's [82] as.

$$\frac{dM_z(t)}{dt} = \frac{M_b^0 - M_z(t)}{T_{1b}} + fM_a(t) - \frac{f}{\lambda}M_v(t) \qquad (2.10a)$$

where the f is the blood flow (CBF) and it can be derived as,

$$CBF = \frac{60 \times 100 \times \Delta M \times \lambda \times R1_a}{2 \times \alpha \times M_c \times \exp(-w \times R1_a) - \exp(-(t+w) \times R1_a} \qquad (2.10b)$$

where $R1_a(0.41)$ is the longitudinal relaxation rate of blood at 9.4T, $M_c$is the equilibrium magnetization of brain, ΔM is the signal difference between labeled and control images,

α (0.96) is the tagging efficiency , t is the delay time between end of RF pulse and start of excitation, and λ (0.9) is blood/tissue water partition coefficient.

2.1.4 Instrumentation Basics

A local brain temperature manipulation system which can manipulate the brain temperature accurately and quickly is necessary for our hypothermia studies.

The local brain temperature manipulation device is composed of four units: a center control unit, which is realized by the BASIC Stamp Chip and related circuit; the A/D&D/A interface unit, which is realized by TLV5616C and TLC2543 chips; the optical communication interface circuit; and Relay and Pump Control unit. For the MR compatible consideration, the device was separated into two parts. The cooling and heating unit is placed inside the MR scanner room, while the electrical control units are placed outside. The optical signal communication was utilized between the two units.

The BASIC STAMP is a microcontroller with a small, specialized BASIC interpreter (PBASIC) built into Read Only Memory (ROM). STAMP can be seen as a small computer, with limited memory, computing ability and interfaces. It provides 12 digital output ports and input ports, which can be used to communicate with other digital devices.

TLV5616 is a 12-bit voltage output digital-to-analog converter (DAC) with a flexible 4-wire serial interface. The 4-wire serial interface allows glueless interface to several kinds of serial ports. The TLV5616 is programmed with a 16-bit serial string containing 4 control and 12 data bits.

TLC2543 is a 12-bit switched-capacitor, successive-approximation, analog-to-digital converters. Each device, with three control inputs, the input-output clock, and the address input is designed for communication with the serial port of a host processor or peripheral through a serial 3-state output. The device allows high-speed data transfers from the host.

The optical communication interface circuit was composed of optical-electric converter, comparator, inverter, amplifier and driver, LED light, optical fiber, etc. It converts the

electrical digital signal to optical signal and provides the communication between the units inside and outside the MR scanner room.

The Relay and Pump Control circuit was composed of D/A converter, amplifier, driver and Relay (Pump). It converts the digital command to analog signal to control the relay and pumps.

2.2 Methods and Design

2.2.1 Animal Surgery Protocols

In this study, MCAO model was used to induce stroke and reperfusion. Adult male Long-Evans rats (280-350g) were used for all proposed studies. The animals were anesthetized with isoflurane (inhaled, 5% induction, and 1.5% maintenance). Thermal stability (37 ± 0.5^{0}C) was maintained with a servo-controlled water pad connected to a rectal thermometer during surgery. Surgical procedures for the intraluminal suture model are similar to that described in [83]. Under general anesthesia, local anesthesia (2% lidocaine hydrochloride) is applied by sub-dermal infiltration of the skin and musculature of the ventral cervical region. The right common Carotid Artery (CCA) and External Carotid Artery (ECA) are exposed through a ventral midline incision. The right proximal ECA is then be ligated permanently. A 4-0 nylon monofilament with its tip coated by silicone is inserted through an arteriotomy of the CCA approximately 3mm below the carotid bifurcation. The suture is secured but can be freely advanced. The incision is closed. The animals are moved into the MR scanner room. After acquiring baseline images, the suture is advanced into the internal carotid artery roughly 20-22 mm until resistance is felt while animals are lying inside the scanner. The continuous different MR sequences are run for the desired time. Reperfusion is achieved by carefully withdrawing the suture from the origin of Middle Cerebral Artery (MCA)/Anterior Cerebral Artery (ACA).

2.2.2 Local Temperature Manipulation Instrument Design

To manipulate the brain temperature, while maintaining a normal body temperature, an MR compatible temperature manipulation device was devised and the diagram is shown in figure 3.

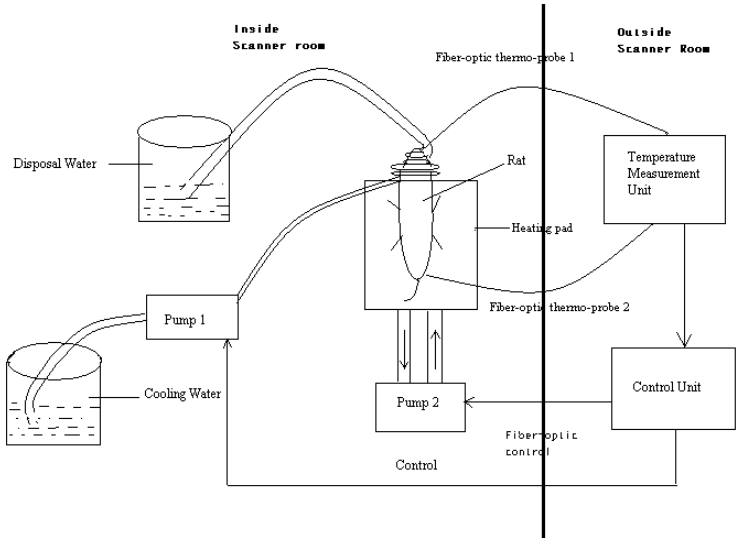

Figure 3. The diagram of the local temperature manipulation system

The MR compatible temperature manipulation device controls the brain and body temperatures separately and simultaneously. The brain temperature manipulation component consists of a tubing coil, which wraps around the head of the rat, a feed-back control unit and an MR-compatible peristaltic pump (SCI400D/U1, Watson Marlow Inc.). Water circulating in the tubing coil was driven by the peristaltic pump. Hypothermia and hyperthermia were induced by using either icy (4℃) or warm water (52℃), respectively. Brain temperature measured with a fiber-optic thermo-probe (Luxtron Inc, Santa Clara, CA) inserted into the brain at a depth of 4.0 mm was utilized by the feedback control unit to adjust the flow rate of the pump so as to induce or maintain the targeted temperature. The body temperature was maintained through a separate feed-back control of the heating pad, which wrapped around the animal body, and a pump. The core body temperature reading from a thermo-probe inserted 4.0cm into the rectum was used as the feedback signal to maintain the desired body temperature at 37.5±0.5℃ by switching the pump on or off. Normothermic condition in the

brain was achieved by adjusting the core body temperature to the normal physiological range with the heating pad.

The key components of the system are the control unit and A/D & D/A interface circuit, together with optical communication interface circuit and relay control circuit. A diagram of the Control units, interface circuit and optical communication circuit are shown in figure 4a to figure 4d.

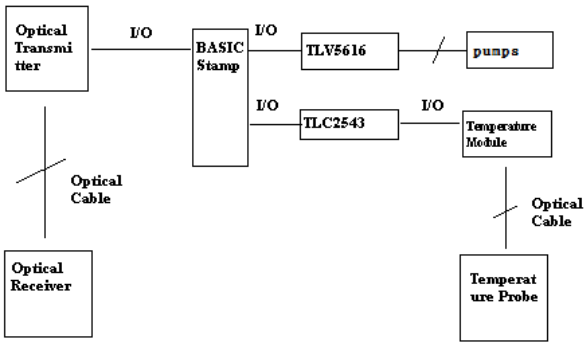

Figure 4a. The Control Unit

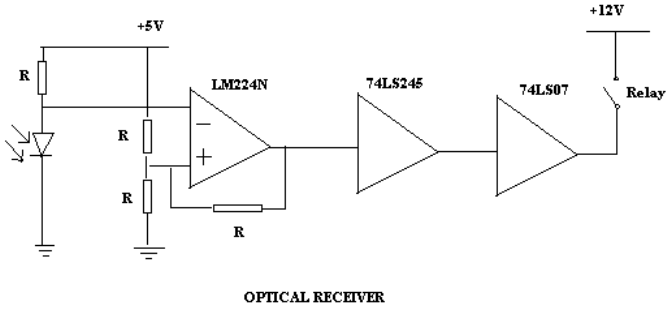

Figure 4b. Optical Receiver

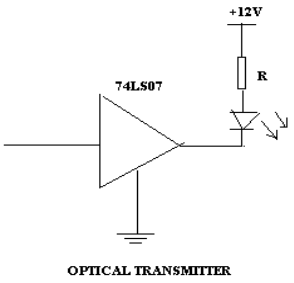

Figure 4c. Optical Transmitter

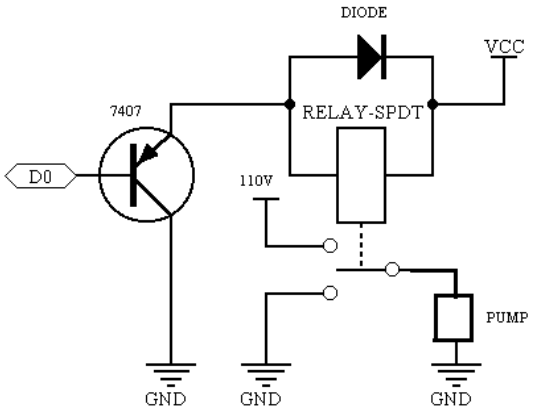

Figure 4d. Relay and PUMP control Circuit

2.2.3 Temperature Manipulation, Measurements of Relationship Between T1 Relaxation vs. Brain Temperature, CBF vs. Temperature, and Temporal Muscle Temperature vs. Brain Temperature

A total of 16 rats were studied and these rats were divided into three groups. Rats in the first group (n=9, 300±25g) were employed to determine the effectiveness of brain temperature manipulation using the devised system. Five different brain temperature manipulations,

hyperthermia (39℃), normothermia (37℃), hypothermia (35℃ and 32℃) and a three-phase hypothermia (29℃, 32℃ and 35℃) were conducted in each rat. For the three-phase hypothermic condition, the brain temperature was first cooled down to 29℃, maintained for 30 minutes, rewarmed to 32℃, maintained for another 30 minutes, rewarmed to 35℃ and maintained for 30 minutes. For the second group of rats (n=5, 300±25g), cerebral ischemia was induced using an intraluminal suture Middle Cerebral Artery Occlusion (MCAO) model under the normothermic condition for 40 minutes, followed by the induction of three different hypothermic conditions, including 35℃, 33℃ and 31℃. In addition, Mean Arterial Blood Pressure (MABP) and Heart Beat Rate (HBR) were recorded through a femoral artery catheter with a blood pressure analyzer (Micro-Med, Louisville, KY). In order to determine how hypothermia affects cerebral perfusion, ADC and CBF maps were acquired at each temperature point. A segmented SE EPI DWI sequence and a continuous arterial spin labeling (CASL) sequence with segmented EPI readout were used to obtain ADC and CBF maps, respectively. Finally, for the sham operated group (n=2, 300±25g), a similar experimental procedure without occluding MCA was performed. The imaging parameters for the segmented SE DWI EPI were as follows: FOV= 45 x 45 cm, 114 x 128 matrix, TR= 1200 ms, bandwidth 592Hz/pixel, and slice thickness 2mm and the imaging parameters for the CASL were: FOV= 45 x 45 cm, 60 x 64 matrix, TR= 3000 ms , bandwidth 1116Hz/pixel, and slice thickness 2mm.

For the ischemic rats (Group 2), three ROIs (core, mismatched and contra) were manually determined based on ADC and CBF maps. The core region was defined as the regions with ADC abnormalities (<mean-3*SD of the contra-lateral hemisphere). The mismatched region was defined as the hypoperfused region without the ADC lesion in the ipsilateral hemisphere. A mirror ROI in the contralateral hemisphere was chosen as the contra ROI. In contrast, an ROI encompassing both hemispheres excluding the region at a proximity to the temperature probe was outlined as sham ROI for rats in Group 3.

To study the relationship between T1 and brain temperature, 5 Long Evan rats were studied. Different brain temperature was induced with our MR compatible temperature

manipulation system. The brain temperature was manipulated from 37 ℃ to 35, 32 and 29 ℃ sequentially. The temperature was maintained at each hypothermia level for 20 minutes and the Look-locker sequences were acquired. A thermo probe is inserted into the brain with a depth of 4.0mm for a direct temperature measurement. T1 maps were calculated with the approach outlined in the theory section. Since the insertion of a thermo-probe may cause brain tissue damage and result in potential signal variation in T1 maps, an ROI placed at a similar location in the contra-lateral hemisphere is used for estimating T1. We assume that the brain temperature gradient caused by the surface temperature regulation is similar in both hemispheres. A linear correlation between the mean T1 from the ROI and thermo-probe measurement was determined.

To study the relationship between the temperature in the temporal muscle and brain, 9 normal rats (280-330g) were used for testing. The same procedures outlined above for local cooling of the brain to 32 ℃ were used. An additional optical thermal probe was inserted 10mm into the cleft between skull and temporal muscle. The temperature of brain and temporal muscle were recorded simultaneously for 90 minutes after the temperature becomes stable.

2.3 Experimental Results

2.3.1 Local Brain Temperature Manipulation

As shown in the results below, our MR compatible local brain temperature manipulation device achieves the targeted brain temperature within 10 minutes and maintains it for 90 minutes. As demonstrated in left diagram in figure 5, five different levels of targeted temperatures (39 ℃, 37 ℃, 35 ℃, 32 ℃ and 29 ℃) were achieved promptly (< 10 minutes) and maintained for 90-120 minutes with a small variation (<0.5 ℃). The rectal temperature remained in the normal range of 37.5 ℃±0.5 ℃ for all rats. Both MABP and HBR resided within their normal levels for all manipulation (Table 1).

	MABP mmHg		HBR	
	Before	After	before	After
Rat1 (39 ℃)	76.0	80.0	367	372
Rat2 (37 ℃)	76.5	72.5	388	375
Rat3 (35 ℃)	70.0	70.0	367	372
Rat4 (32 ℃)	77.0	73.0	370	340
Rat5 (29 ℃)	74.8	71.5	381	337

Table 1. MABP and HBR measurement before and after temperature manipulation

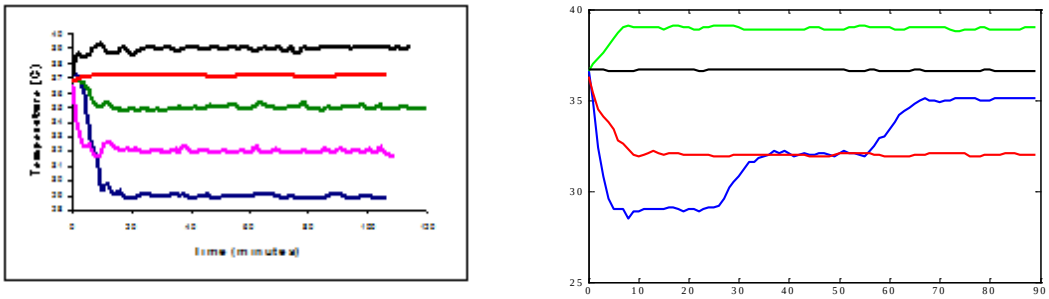

Figure 5. The manipulation of brain temperature. Left, Five target temperature (39, 37, 35, 32 and 29 ℃); Right, continuous manipulation of brain temperature from 29 to 32 and then to 35 ℃ (blue).

As shown in the right diagram in figure 5, the blue curve shows the three-phase brain temperature manipulation. First, 29 ℃ targeted temperature was achieved within 10 minutes and maintained for 20 minutes, then it rewarmed to 32 ℃ within 10 minutes and maintained for another 20 minutes, and final rewarmed to 35 ℃ and maintained for the rest 20 minutes. The rectal temperature keeps within the normal range during the whole period of time.

2.3.2 Relationship Between Temporal Muscle Temperature and Brain Temperature

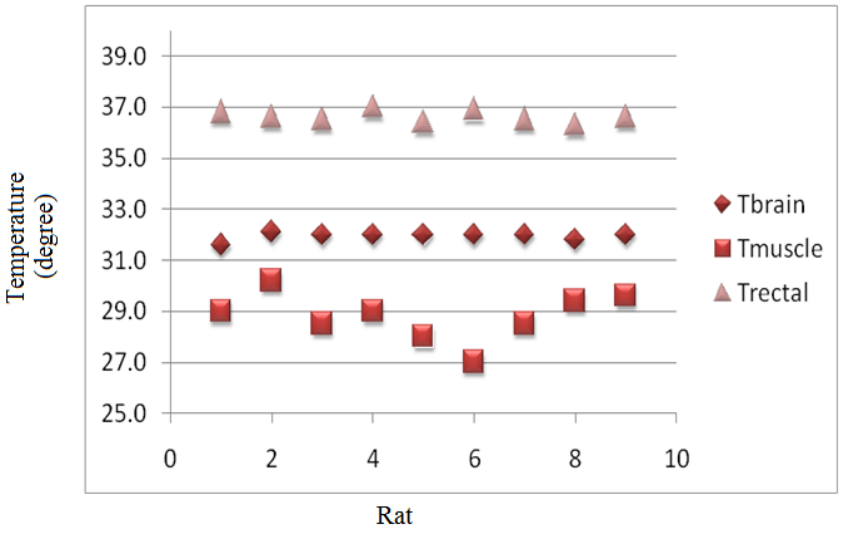

Figure 6. The temperature of the brain, temporal muscle and rectal under local cooling of the brain to 32 ℃ (9 rats totally)

In this study, there is no consistent temperature relationship between temporal muscle and brain across animals. As shown in figure 6, the difference of temperature can be as low as 2℃, but also as high as 5℃. If considering each animal individually, the difference is stable for as long as 90 minutes. Figure 7 shows a typical relationship between temperature in the temporal muscle and brain from one rat with a targeted temperature of 35℃. The temperature difference is around 2.0 ℃ and is stable during the 120 minutes,

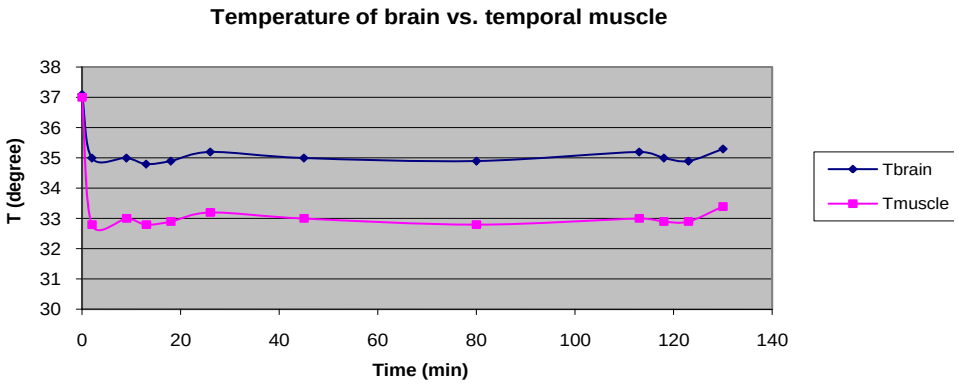

Figure 7. The relationship between the temperature of temporal muscle and brain during a 90 minutes study

2.3.3 Correlation Between T1 and Brain Temperature

Spin-lattice relaxation time (T1) has been demonstrated to be linearly proportional to temperature when it is below 45 ℃ [79-81]. Our results demonstrated that a highly linear correlation (y=0.011x-0.0003, R=0.94) exists between change of T1 and change of brain temperature (29 ℃-37 ℃) in the gray matter of brain, as shown in figure 8.

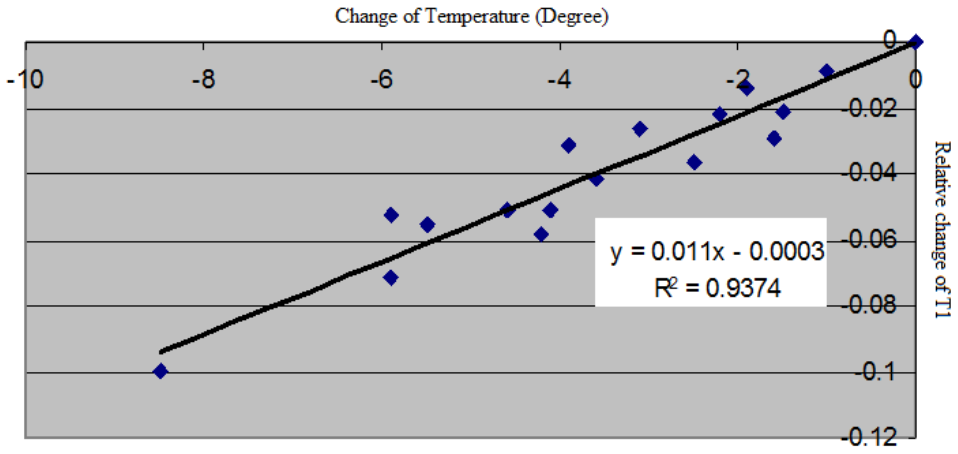

Figure 8. Changes of relaxation T1 vs. changes of Temperature in the subcortical and cortical region

This correlation can be utilized to obtain relative temperature maps in the brain. In this study, the temperature under a normothermic condition prior to any temperature manipulation is utilized as the reference temperature. The T1 maps prior to and after temperature manipulation can be derived by the TOMROP sequence. A pixel-by-pixel brain temperature mapping can then be calculated using the relationship between T1 and temperature derived previously.

2.3.4 Relationship Between CBF and Temperature

2.3.4.1 Typical CBF Changes Under Normothermia Condition with MCAO Model

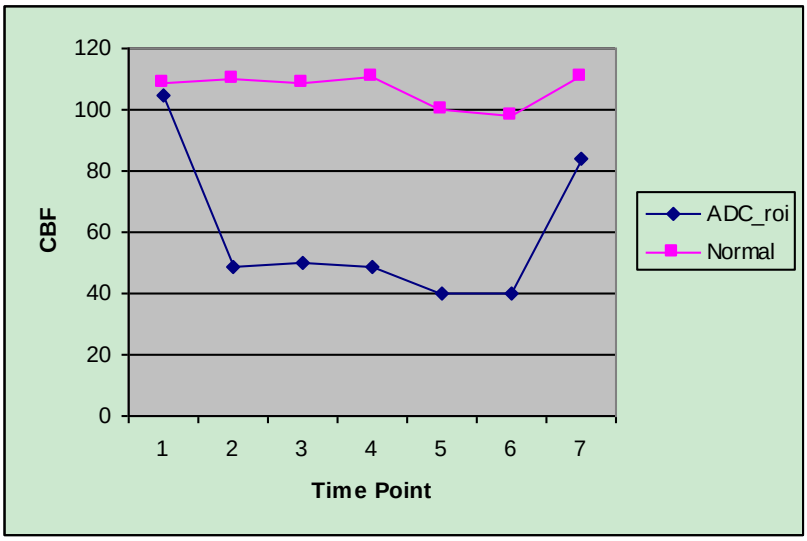

Figure 9. Typical changes of CBF under MCAO

A typical diagram of CBF under MCAO model is shown in figure 9. The CBF decreased immediately after the occlusion, remained stable during the occlusion and then recovered back to slightly below normal after reperfusion.

2.3.4.2 CBF Under Hypothermia Condition with MCAO Model

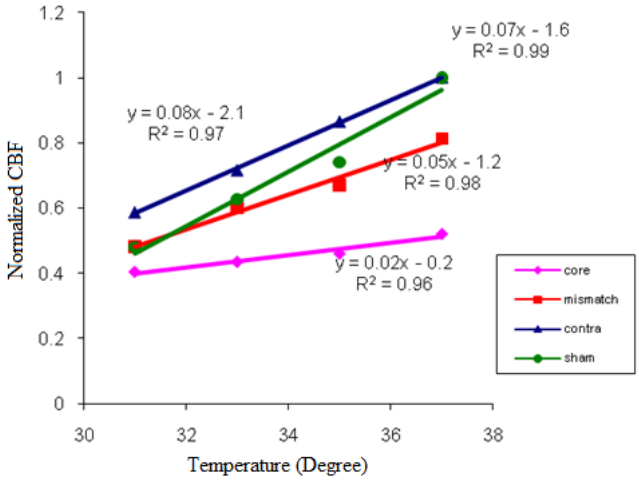

Figure 10. The changes of CBF with temperature in different region on normal rats

The relations between CBF and the brain temperature under ischemia are shown in figure 10. Cooling the brain always resulted in decreases in CBF at different regions. A highly linear relationship is observed between CBF and the brain temperature independent of the brain perfusion status. However, the rate of CBF reduction in response to hypothermia differed among different ROIs. The CBF in the sham group (circle) drops most rapidly, followed by the contra region (triangles), mismatch region (squares) and the core region (diamonds).

2.4 Conclusion and Discussion

The local brain temperature manipulation system can manipulate the brain temperature of rats quickly and accurately while at the same time, maintaining the body temperature and physiology parameters within normal range. The results showed that the targeted temperature was reached within 10 minutes and kept for long period of time (>90 minutes), with a small variation (less than 0.5℃). The system is also MR compatible to be used for MR scanning.

The efficiency of local cooling depends on both the temperature of the cooling water and the rate of water flow. For this device, the temperature of cold water was found to be the major factor that decides the cooling efficiency, while adjustment of the rate of water flow was utilized as fine adjustment. For each targeted temperature, different temperature of cooled water is manually preset (4 ℃ for 29 ℃ target temperature, 10 ℃ for 32 ℃ and 20 ℃ for 35℃). At the beginning of cooling, a high speed of water flow was used to initialize the cooling process. After the temperature is within 2 ℃ of the target temperature, the rate of water flow is decreased slowly to approach the target temperature. The brain temperature can be maintained within 0.5 ℃ of targeted temperature by fine adjustment of water flow.

Although surface local cooling reduces the side effects compared to the global cooling, such as shivering, arterial hypotension, etc., it induces temperature gradient within the brain. . The magnitude of the gradient depends on multiple variables, including tissue heat conduction, blood flow, body temperature, ambient air temperature, etc. In our study, in order to reach 29 ℃ deep inside brain, the surface of head has to be cooled to about 10℃. Similar

result was reported by Abbot et al [84]. Given the temperature gradient within the brain tissue, our T1 based MR temperature mapping method will be used to measure the temperature distribution within the brain.

For this device, a thermo probe is required as the real time feedback signal. Since a direct measurement of brain temperature with a thermo-probe causes tissue damage and induces susceptibility artifacts in MR images, the temperature in temporal muscle can be utilized. Recent global cerebral ischemia and head injury rat studies have utilized this approach. However, the temperature in temporal muscle can differ from that in the brain, particularly during ischemia (57), (34). Moreover, surface cooling may cause a large temperature difference between the temporal muscle and brain. In our study, we found there temperature difference between temporal muscle and brain ranged from 2 ℃ to 5 ℃ across different animals. Two possible reasons may explain it. Firstly, since there is a large temperature gradient under surface cooling, the temperature measurement is very sensitive to the position of the probe between temporal muscle and skull. A small difference in location may result in very different temperature measurements. Secondly, the space between the cooling coil and the head of animal might vary for different animals. Since air has high heat impendence, a small difference of the space will cause a large difference of temperature. Nevertheless, although the temperature difference between temporal muscle and brain varies from animal to animal, it remains very stable for a long period of time for each animal. This stable relationship motivates us to use temporal muscle temperature as the feedback control signal to keep the brain temperature stable for a desired period of time. Since MR method can be used to derive the brain temperature after data acquisition, we can classify the animals to different hypothermia groups according to their brain temperature maps at the later data analysis stage.

A highly linear relationship between T1 and local brain temperature was found in the study in normal rats, which can be utilized for measurement of brain temperature under hypothermia condition. One problem will happen if we want to apply the T1 map method to measure the temperature in stroke. Although there is no significant change of T1 reported

under a magnetic field <3T in the acute stage of stroke, a rapid increase of T1, as large as 9%[85-88] within 10 minutes after occlusion was reported using a high magnetic field. Moreover, T1 continues to elevate for the next 60 minutes. This increase in T1 occurred immediately after stroke onset. Vasogenic edema that normally occurs a few hours or days after ischemia is not the primary reason. Since the inflow of fresh blood may contribute to a faster apparent T1 recovery[89], one plausible explanation is that the decrease of blood flow may reduce the apparent T1. However, the continued elevation of T1 within one hour after stroke cannot be explained since CBF remained stable during the same period of time. In addition, the maximum signal change caused by a completely stopped flow would be only 3% based on an analytical calculation. Another possible reason is the rapid increase of temperature which induces an increase of T1 after the onset of stroke. While it has been reported that the temperature in the ischemic region decreases, since the reduction of the blood flow[90] blocks the warm blood from entering the ischemic region. However, on the other hand, blood flow also carries away the heat generated by tissue metabolism and a reduced blood flow may result in a local increase of temperature. Thus far, the exact mechanism why T1 increases acutely is not known. The pathological induced T1 increase may confound the measurement of brain temperature. Assuming the temperature distribution within the brain is symmetric across hemisphere, the T1 measurements from the contralateral unaffected hemisphere will allow a brain temperature mapping.

A highly linear relationship between CBF and brain temperature was found in our study. The local cooling to produce hypothermia in the rats consistently reduces CBF in normal region. This finding is consistent with that previously reported by Laptook, A. R. et al[84]. They reported that the decrease of temperature about 4 ℃ (body cooling) resulted in a reduction of 40% of CBF of control. In our study, a similar result was observed; a 40% decrease of CBF leads to a temperature drop from 37 ℃ to 33 ℃ with surface cooling.

A highly linear relationship between CBF and temperature was also observed in the infarct region. However, the rate of CBF reduction differs under different severities of

occlusion. Although many physiological possibilities may account for the observed different relations between CBF and the brain temperature, it is plausible that the status of autoregulation plays a critical role on how CBF will respond to brain temperature manipulation; the autoregulation is dysfunctional in the core area while may be slightly impaired in the mismatched regions, leading to different CBF characteristics in responses to temperature manipulations. More studies are needed to further investigate whether or not brain metabolism under hypothermia also responds in a similar manner as that of CBF.

CHAPTER 3

R2' MEASUREMENT AND ANALYSIS OF MULTIPLE MR PARAMETERS IN MCAO

3.1 Theory: the Related MR Principles

3.1.1 Introduction of DSC Method to Measure CBF

Perfusion measurements by Dynamic Susceptibility Contrast (DSC) magnetic resonance imaging utilize very rapid imaging (most commonly Echo Planar Imaging (EPI)) to capture the first pass of intravenously injected paramagnetic contrast agent - bolus tracking. By kinetic analysis, hemodynamic parameters, such as Cerebral Blood Flow (CBF), Cerebral Blood Volume (CBV), and Mean Transit Time (MTT), can be derived.

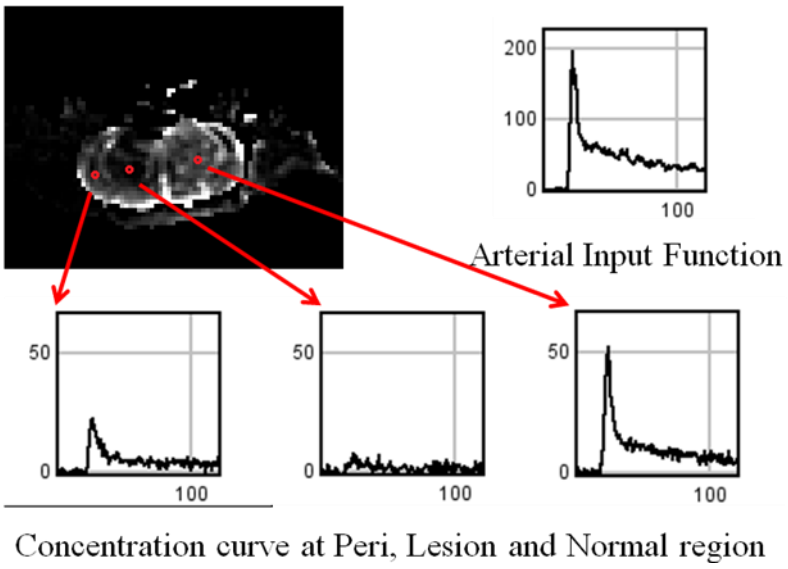

Figure 11. The dynamic concentration curve of the DSC method

Assuming a linear relationship between concentration of a high magnetic susceptibility contrast agent and change in transverse relaxation ($\Delta R2$) in dynamic susceptibility contrast-weighted (DSC) MR imaginings[91], the change in concentration over time during the passage of a bolus of contrast agent in a volume of tissue $c(t)$ can be characterized as:

$$C(t) \propto \Delta R_2(t) = -\frac{1}{TE} \ln \frac{S(t)}{S_0} \tag{3.1}$$

where S_0 is the baseline MR intensity, and $S(t)$ is the signal intensity over time. Typical concentration curves after ischemic stroke are shown in figure 11.

By defining the residue function R(t) as the fraction of tracer remaining in the system at a given time t, the concentration of tracer within the voxel of tissue as can be modeled as

$$C(t) = F_t C_a(t) \otimes R(t) = F_t \int_0^t C_a(\tau) R(t-\tau) d\tau \tag{3.2}$$

where $C_a(\tau)$is the Arterial Input Function (AIF) and F_t is the tissue blood flow. The AIF is typically measured directly from the MR images within an arterial vessel. R_t can then be estimated using deconvolution with the measured $\Delta R_2(t)$, which is often performed using the Singular Value Decomposition (SVD) method[92].

The equation (3.2) can be expressed in a discrete format:

$$c(t_j) = \Delta t . F_t . \sum_{i=0}^{j} C_a(t_j) . R(t_j - t_i) \quad (3.3)$$

where Δt is the sampling interval and expanding equation into matrix notation, the deconvolution problem can be formulated as an inverse matrix problem,

$$\begin{bmatrix} C(t_0) \\ C(t_1) \\ \vdots \\ C(t_{N-1}) \end{bmatrix} = \Delta t \begin{bmatrix} C_a(t_0) & 0 & \cdots & 0 \\ C_a(t_1) & C_a(t_0) & \cdots & 0 \\ \vdots & \vdots & \ddots & \vdots \\ C_a(t_{N-1}) & C_a(t_{N-2}) & \cdots & C_a(t_0) \end{bmatrix} \times \begin{bmatrix} R(t_0) \\ R(t_1) \\ \vdots \\ R(t_{N-1}) \end{bmatrix} \cdot F_t \quad (3.4)$$

Simplifying the above equation to $c = A.b$, one can solve for b, which is R(t) scaled by F_t. By decomposing $A = U \cdot S \cdot V^T$, where U and V are orthogonal matrices and S is a nonnegative square diagonal matrix, the inverse can be expressed as $A^{-1} = V \cdot W \cdot U^T$ where W=1/S along the diagonals, and zero elsewhere. Values of W corresponding to values where S is less than a preset tolerance threshold $(TH_{svd} = 0.2)$ are set to zero. The residue function scaled by F_t and b, can then be estimated by $b = F_t V \cdot W \cdot U^T \cdot c$, and rCBF is estimated as b's maximum value.

3.1.2 The Blood-Oxygen Level Dependent (BOLD) Related Concepts

3.1.2.1 Paramagnetic, Diamagnetic and Ferromagnetic

An atom with an unpaired electron has a nonvanishing permanent magnetic moment with an associated nonzero dipole magnetic field, and is referred to as 'paramagnetic.' While these moments would be randomly distributed in the absence of outside interaction, it tends to align with an external magnetic field, producing a bulk magnetic moment and a corresponding macroscopic magnetic field augmenting the external field.

Whether or not there are any permanent magnetic dipole moments, all materials will introduce dipole moment in the presence of time-dependent external magnetic fields. This is a much weaker effect than paramagnetism, and is called 'diamagnetism.' In those cases where the electrons pair up to cancel their spin magnetic moments, diamagnetism dominates the effect. In diagmagnetism, the macroscopic sum of the induced moments is roughly anti-

parallel to the external magnetic field, and its macroscopic field opposes weakly the eternal magnetic field.

Certain materials have permanent domains of electron spin magnetic moments which continue to produce a very strong macroscopic field independent of the external magnetic field. The domains are randomly distributed throughout the material unless there is an external field. When they are aligned by the temporary application of an external field, a permanent macroscopic magnet is produced. Iron oxide particulates are an example of such super paramagnetic materials. Thanks to the large local fields created, ferri oxide or iron particles are used as a contrast agent to produce signal loss in regions where they are deposited or to which they have migrated. A single particle can affect the signal in a volume millions times larger than the original particle volume.

Blood can be approximated as a two-compartment system containing both plasma and red blood cells. The fraction of the volume of packed red blood cells to the volume of whole blood is called the hematocrit (Hct), which is typically about 0.4 (40%).

It is well known that as oxygen content in blood changes so does the local susceptibility in the blood. The source of this has been shown to be the unshielded iron in hemoglobin (red blood cells). Much of the iron in the blood is in the hemoglobin, or more specifically, in one of two states, oxyhemoglobin or deoxyhemoglobin. These two states differ in their magnetic properties. Oxyhemoglobin is diamagnetic with no unpaired electrons. A deoxyghemoglobin molecule has unpaired electrons and is paramagnetic. The different magnetic properties between these two provide a potential contrast depending on blood oxygenation level, which is called Blood oxygenation level dependent (BOLD) contrast.

In the brain, the blood vessels can be seen as a network of long cylinders (compared to the radius) with random orientations. Yablonskiy and Haacke [93] proposed an analytical model characterizing MR signal without intravascular signal contribution. The MR signal can be written as below,

$$S(t) = \rho.(1-\lambda).\exp\left[(-\lambda.f_c(\delta\omega t)\right] \quad (3.5)$$

where

$$f_c(\delta\omega t) = 1/3.\int_0^1 (2+u).\sqrt{1-u}.\frac{1-J_0(\frac{3}{2}.\delta\omega t u)}{u^2}du \quad (3.6)$$

where ρ is the spin density, λ is the volume fraction, $\delta\omega$ is the processing frequency in the magnetic field, t is the signal decay time, and J_0 is the zeroth order Bessel function. If one assumes that the arterial blood is fully oxygenated, then the $\delta\omega$ can be further derived from

$$\delta\omega = \gamma.\frac{4}{3}.\pi\Delta\chi_0.Hct.OEF.B_0 \quad (3.7)$$

where γ is the gyromagnetic ratio, which equals to $2.675 \times 10^8 rad/s/Tesla$; Hct is the fractional hematocrit; B_0 is the main magnetic field strength; $\Delta\chi_0$ is the susceptibility difference between fully oxygenated and fully deoxygenated blood which has been measured to be 0.18ppm per unit Hct in cgs units; and OEF is the oxygen extraction fraction.

Based on their model, the relaxation R2′ is linearly proportional to OEF and can be written as follow[94]:

$$R2' = \lambda \cdot \delta\omega \propto \lambda \cdot OEF. \quad (3.8)$$

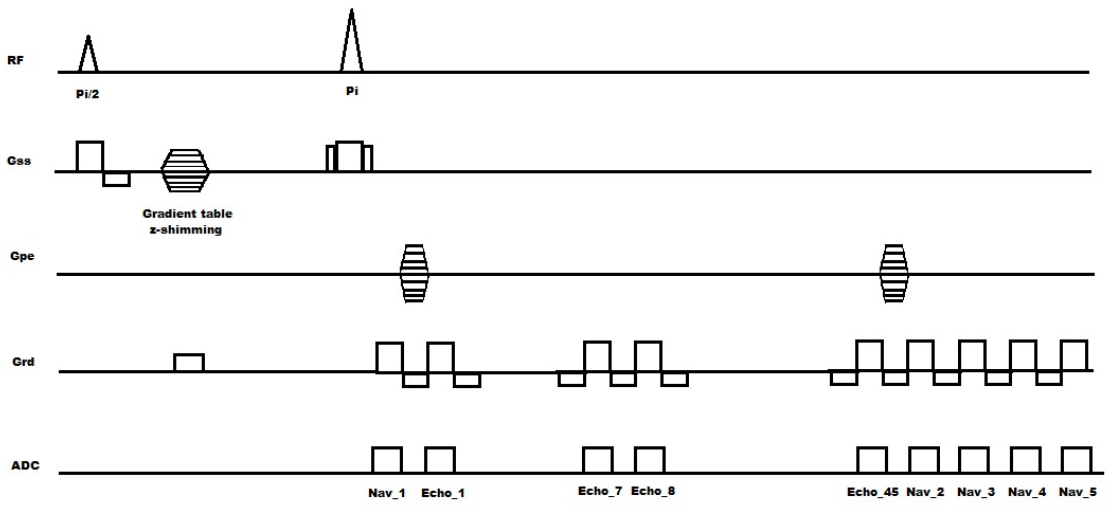

Figure 12. GESSE sequences diagram

A two dimensional, multi-echo gradient/spin echo sequence can be used to acquire images. As shown in figure 12, 45 echoes, with echo spacing 1.79 ms, are acquired after

180° RF pulse. The spin echo occurs at the middle of the 7th and 8th echo, which is optimized for calculation of R2' (see results section for detail). The R2 were calculated by using the 7 symmetric pairs of echoes around the spin echo. After removing the R2 component from the signal, the R2' and γ can be estimated by fitting the images using the analytical model with a matching filter method.

3.1.3 Correction of Motion

The bulk motion of an object during data acquisition causes an inconsistency in phase along the phase encoding direction which results in ghosting artifact in the image. An approach which combines pulse sequence design and post processing has been proposed by Ordidge et al.[95]. In this approach, a two echo-pulsed gradient spin-echo (PGSE) experiment is performed. The first echo, which is called navigator echo, is not phase encoded, while the second echo, the imaging echo, is phase encoded in the usual manner. Both the navigator and regular echoes contain the same undesirable effects of patient motion. Since there is no phase encoding gradient for the navigator echo, ideally, any variation of phase of the navigator echo from one phase encoding line to another is due to the motion. Thus, this motion-induced phase error, relative to the reference phase encoding line, can be found by subtracting the phase of the reference encoding line from other phase encoding lines. Then these phases differences can be added back to the image echo of each encoding line and thus correct the motion.

The k-space signal can be described as below[96, 97],

$$M(k_x,k_y) = \iint m(x,y)e^{-2\pi i(k_x x + k_y y)}\,dxdy \qquad (3.9)$$

where m(x,y) is the spatial distribution of magnetization and k_x and k_y are the k-space spatial frequency terms which are proportional to the gradients G_x and G_y, respectively. The navigator echo is obtained by acquiring the echo without a phase encoding gradient,

$$NAV(k_{ref}) = M_{ref}(k_x,0) = \iint m(x,y)dye^{-2\pi i(k_x x)}\,dx \qquad (3.10)$$

When a rigid-body motion occurs along the phase encoding direction during image acquisition, an extra phase term is added to each k-space line along phase encoding as below,

$$M'(k_x, k_y) = M(k_x, k_y) e^{i\Delta\phi(k_y)} \quad (3.11)$$

where the phase difference can be calculated with the navigator echoes,

$$\Delta\phi(k_y) = \arg[NAV(k_y)] - \arg[NAV(k_{ref})] \quad (3.12)$$

where arg is the phase of a complex signal.

There are 45 image echoes in the GESSE sequence, with the longest TE acquired at 90 ms. One navigator echo at the beginning of the sequence cannot represent all the phase variation, especially at the longer TE echoes. To solve this problem, four addition navigator echoes were added after all image echoes, as shown in figure 12. The phase variation of each image echo was determined by linear fitting of the phase differences of the 5 navigator echoes.

3.1.4 Correction of Static Magnetic Field Variations

The B0 field inhomogeneity is the source of distortion in both SE and GE sequences and signal loss in GE sequences, which usually occurs in regions of the brain adjacent to air cavities such as in the frontal orbital or lateral temporal areas. The susceptibility-induced B0 inhomogeneity is proportional to the magnitude of the magnetic field. Although a higher magnetic field increases the sensitivity for studies that utilize the mesoscopic B0 inhomogeneity, e.g. fMRI and OEF, the susceptibility effect from high macroscopic B0 inhomogeneity also becomes more apparent.

In general, the B0 inhomogeneity is linear or at a low order. Since in MRI, the dimension along z direction is usually larger than the other two directions, it usually has the largest intravoxel phase dispersion along the z direction. Thus, in the following sections, only the susceptibility-induced gradient along z direction is considered.

A double echo 3D gradient echo sequence can be used to calculate the B0 inhomogeneity. The difference of disturbed B0 field from the original B0 field (dB) induces an additional phase, which is proportional to the B0 inhomogeneity and the echo time TE. To derive the magnitude of the B0 inhomogeneity, the subtraction of the phases of the two echoes can be

utilized. Usually the complex division method is preferred to reduce the phase wrap problem[98].

$$\Delta B = angle(C_2 \exp(i\phi_2) * conjugate(C_1 \exp(i\phi_1))) / (\gamma . \Delta TE) \quad (3.13)$$

where ΔTE is the echo time difference between the two echoes.

Several methods have been proposed to correct the B0 field inhomogeneities. Basically, these methods can be categorized into five categories. The comparisons of these methods are shown in table 2.

	Summary	cons
Thinner slices/higher resolution	Excitation of thinner slice thickness	Extreme small thickness are needed Compromised SNR Longer acquisition time or Reduced spatial coverage Higher hardware requirement(Gradient, RF pulse)
Tailored RF pulse	Application of quadratic phase of RF pulse, added to the linear phase produced by B0 inhomogeneity	Low SNR (1/2 of original SNR) Need careful calculation and specific design of RF pulse
Passive shimming	Induce additional dB field to compensate the susceptibility induced B0 inhomogeneity with an additional diamagnetic material	Low consistency Hard to control
Post processing method	Use known B0 distribution to correct the signal decay curve	Need pre acquisition of B0 map Won't work for high B0 inhomogeneity
z-shimming method	Application of gradient table on z direction	Lower SNR Reduced the temporal resolution to 1/N

Table 2. Comparison of different B0 inhomogeneity correction methods

The method of Gradient Echo Slice Excitation Profile Imaging (GESEPI) was proposed by Yang et al[99] to correct B0 inhomogeneity. In the conventional 2D gradient echo

sequence, the image intensity is in the center of k space along the K_z direction ($K_z = 0$). With the susceptibility induced linear gradient along z direction, the magnetization distribution along z is as below,

$$MTE(z) = M(z) * \exp(i\gamma.Gz.TE.z) \tag{3.14}$$

where Gz is the susceptibility-induced gradient and TE is the echo time. Based on FFT shift theory, the signal maximum will shift to a new position ($Kz = Knew$) in k space as below

$$F(MTE(z)) = F(M(z) * \exp(i\gamma.Gz.TE.z)) = M(kz - Knew) \tag{3.15}$$

$$Knew = \frac{\gamma}{2\pi}.Gz.TE \tag{3.16}$$

Thus, the conventional 2D acquisition, which only acquires the signal at $K_z = 0$ will miss the signal peak and further induce loss of signal. To compensate this shift of peak, an additional gradient G_c with the same magnitude as G_z but opposite sign can be applied for compensation. This addition G_c moves the signal peak from the position k_{new} back to $K_z = 0$, thus recovers the signal losses. In the GESEPI method, instead of applying one addition gradient along the z direction, a table of compensation gradients was applied, resulting in acquisition of a series of 2D images, with each image has a different amount of compensation effect. A FFT is applied along the z direction and multiple images in spatial domain were calculated. The final output image is calculated by the sum of the multiple slices within the same slice thickness as the conventional GE sequence.

The shift of the signal peak is proportional to the susceptibility induced gradient G_z and the echo time. To compensate the largest shift of signal peak, the maximal compensation gradient in the gradient table should be no less than $G_z * TE_{last}$,

$$Gc\max * tc \geq Gz * TE_{last} \tag{3.17}$$

where $G_{c\max}$ is the magnitude of the maximal compensation gradient and t_c is the duration of compensation gradient table.

3.2 Methods

3.2.1 Consistency Test Protocols

A phantom study was performed to test the effect of z-shimming method. A phantom with air bubble inside was inserted into the bore of a 9.4T scanner. As shown in figure 13, a revised gradient echo sequence (TR/TE:80ms/2.81ms) was utilized to acquire the data, with a compensation gradient table added on the slice selection direction (z-shimming). Sixteen steps of compensation gradient were applied, with shimming FOV 3.2 mm and excitation slice thickness 1.6mm. The excitation slice was chosen along the axial direction, with 20mm distance from the air bubble. The center slice of the 16 slices (Kz=0) and the combined image (average of center 8 slices of the 3rd dimension FFT reconstructed magnitude image) were compared.

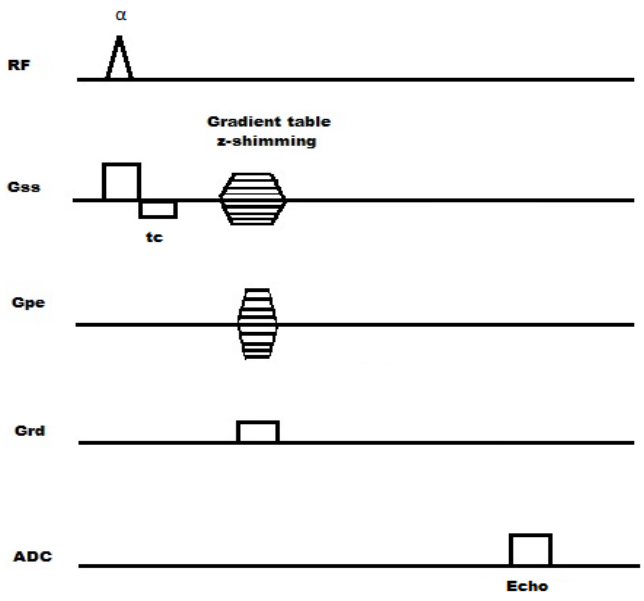

Figure 13. Multiple Gradient Echo sequence with z-shimming method

To test consistency of the R2’ measurements of the method, 6 normal rats were scanned with the GESSE sequences with z-shimming and motion correction applied. The sequence protocol is shown in figure 14. A optimized 2D multi-echo gradient echo sampled spin echo (GESSE) sequence was used to acquire 50 echoes to estimate R2′ . Navigator echoes were added for motion correction. All 50 echoes were equally spaced with an inter-echo spacing of 1.79ms, with the 7th and 8th echo symmetrically placed around where the true spin echo may occur. Field of View (FOV) and matrix size were set to 30x30 mm2 and 96x96, with a slice thickness of 1mm. The repetition time (TR) and echo time (TE) of the first echo were 2000 ms and 17.91 ms. A compensation gradient table was added on the slice selection direction, with shimming FOV is 2.0mm and step number is 6.

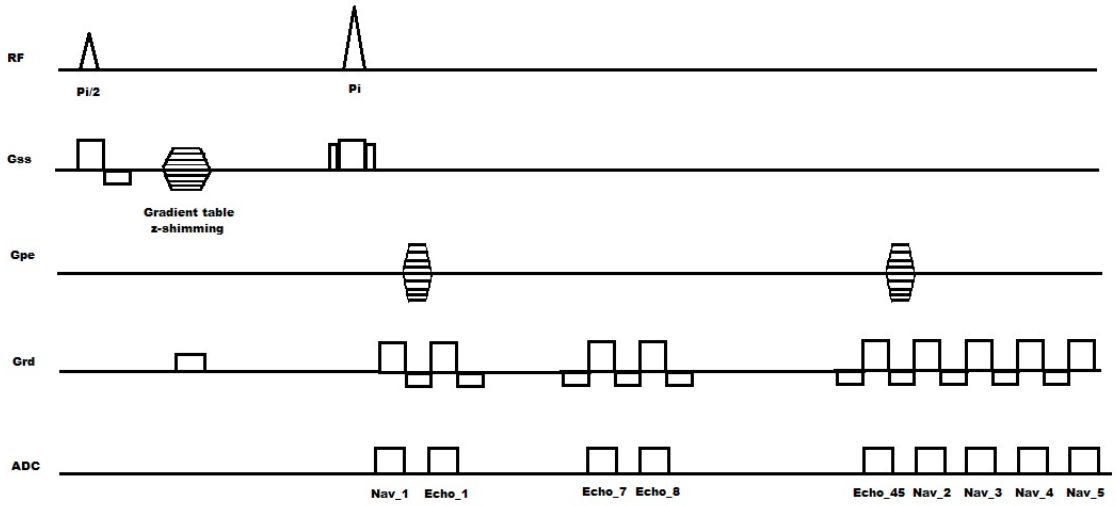

Figure 14. The GESSE sequence for measurement of R2’

As shown in figure 15, totally 12 ROIs with 4x5 voxels each, are defined in the cortical and subcortical areas in both hemispheres symmetrically. The standard deviations of the mean value of each ROI across all the animals were calculated and used to measure the consistency of the method.

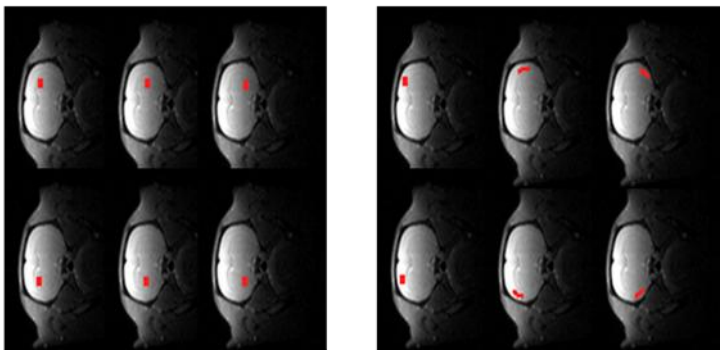

Figure 15. The definition of the ROIs in subcortical (left) and Cortical (right) regions

All MR images were acquired on a Bruker Biospec 9.4T small animal MR scanner (Bruker Medizintechnik, Karlsruhe, Germany) with a surface coil. Field map shimming was utilized to minimize the background magnetic field inhomogeneities. CBF was acquired with a DSC method. 4 doses (0.25ml/300g) of Gadolinium were injected through a tail vein. The images were acquired continuously by an Echo planar imaging (EPI) sequence (TR/TE, 300ms/9.3ms; FOV, 30x30mm; matrix, 96x96; Repetition, 120) with temporal resolution 0.6s. ADC was computed from diffusion weighted images (DWI) acquired with a single-shot spin-echo EPI sequence (TR/TE, 2500ms/100ms; FOV, 30x30mm; matrix, 96x96, two b values: b=0 and 1000 s/mm2 applied in three orthogonal axes). In addition, T2 weighted (T2w) images were obtained with a Rapid Acquisition Relaxation Enhanced (RARE) sequence with nine slices (TR/TE 3000ms/40ms; RARE factor, 10; FOV, 30x30mm; matrix, 192x192). The GESSE sequence is the same as described in the previous section of consistency testing.

GESSE, CASL, DWI and T2w sequences were acquired during acute MCAO immediately followed by a reperfusion. Another T2w images were acquired at the 24 hours after MCAO to identify final infarct.

For the R2' measurement sequence, I made the following improvement in my sequence for motion correction. One navigator echo without phase encoding was added before all the image echoes and another four navigator echoes were placed after the final echo. For data processing, a 1D inverse Fourier transform along readout direction was applied to both the

navigator and regular echoes and translated the data into the hybrid domain (k domain along y direction and image domain along x direction). A point-by-point phase comparison was made between the reference line (48^{th} phase encoding line) and each of the rest of phase encoding lines. The phase difference for the navigator echo (1st, 47th, 48th, 49th and 50th navigator echoes) over time was fitted with a linear model. The phase differences of other image echoes between navigator echoes were derived by the linear relationship and added back to the image echoes. After all the lines were corrected, the inverse Fourier Transform was applied along the phase encoding direction for all the image echoes and the 2D images were reconstructed.

3.2.2 R2' measurement

The GESSE images were utilized to obtain R2′ maps as described in the theory part. As a preprocessing routine, navigator echoes were used to correct for motion artifacts. A 3x3 low pass filter was then applied to improve the signal-to-noise ratio (SNR). R2 maps were calculated by fitting of the seven pairs of echoes symmetrically around the spin echo as described previously . Subsequently, the R2 decay term was removed from the images. R2′ was then obtained with a numerical method (matched filter method) based on an analytical signal model as shown in equation (3.5).

Finally, OMI_ R2′ was computed as the product of CBF and R2p as follows.

$$OMI\_R2' = CBF \times R2' \tag{3.18}$$

The 24hrs T2W images were registered to the T2W images at the acute stage with a rigid transformation for each rat using FSL 3.2 (FMRIB, Oxford, UK). Three different ROIs were defined on the co-registered 24hrs T2W images. The INFARCT ROI was manually delineated as hyperintense regions in the ipsilateral hemisphere. The MIRROR ROI was manually defined as the mirror counterpart of the INFARCT ROI in the contralateral hemisphere. The IPSI ROI and CONTRA ROI were manually defined to encompass the whole ipsilateral and contralateral hemispheres, respectively, without ventricles and white matter. The PERI ROI was then obtained by a subtraction of the INFARCT ROI from the IPSI ROI. For all ROIs,

one pixel along the brain edge was excluded to minimize susceptibility and partial volume effects. Moreover, in order to minimize the potential errors induced by mis-registration and noise induced spurious variations, isolated regions that are smaller than 1 mm3 were not included.

The median value in the CONTRA ROI was utilized to normalize CBF (nCBF), ADC (nADC), OMI_ R2′ (nOMI_R2′) and R2′ (nR2′). In the assessment of each normalized parameter in predicting tissue outcome, two pools of voxels were constructed. The first pool (dead tissue) consisted of all the voxels from the INFARCT ROI and the second pool (alive tissue) consisted of roughly equal number of voxels randomly selected from the PERI ROI (if INFARCT ROI is greater than PERI ROI, some voxels were then randomly selected from the MIRROR ROI). This procedure is necessary for an optimized prediction power. To improve statistical power, data from all animals were pooled together. ROC analysis was then performed for each parameter. The area under the ROC curve (AUC) was used to evaluate the prediction performance of each parameter, with a higher AUC indicating a better prediction. ROC analysis was conducted 500 times to minimize a potential variation caused by the random voxel selection in constructing the live tissue pool and mean AUC was utilized.

The scatter plot maps were drawn to demonstrate the relationship between CBF, ADC, OMI_R2’ and R2’, with all voxel in the ipsi hemisphere, excluding the WM and CSF regions. The ipsi hemisphere was divided into two regions manually, the dead region, which has high intensity in the registered T2w images, and alive region. The scatter plot and analysis are based on the two regions, separately.

Histogram maps of CBF, R2’ and OMI_R2’ were obtained for the time points before reperfusion and after reperfusion from INFARCT, PERI and CONTROL regions.

3.2.3 The decision of the compensation gradient

Experimental results showed that the largest susceptibility induced dB is around 0.05ppm at the edge of the brain. The following calculation is to decide the magnitude of gradient that should be used to compensate the dB at the longest echo time.

For the R2' measurement sequence, the last echo is the 45th echo from spin echo. The longest echo time interval from spin echo can then be calculated as $TE = ((45 - 7.5) \times 1.79ms$

The gradient needed to compensate the susceptibility induced gradient

$$G_{zmax} = 0.05ppm * B0 * \frac{TE}{T_c} = 0.06 * 10^{-6} * 10^3 * 9.4 * (45 - 7.5) * 1.79 * \frac{10^{-3}}{0.21 * 10^{-3}} = 150mT/m \quad (3.19)$$

where $\tau_c = 0.21e-3s$ is the duration of the compensation gradients, the maximal compensation gradient is calculated as

$$G_{cmax} = \frac{1}{2 * 10^{-3}} * \frac{3}{\gamma} * \frac{2\pi}{tc} = 167.7mT/m \quad (3.20)$$

This maximal compensation gradient fulfills the requirement to compensate the largest phase dispersion at the longest echo time. The compensation gradient table has 6 steps, resulting in a FOV of 2 mm in the z direction.

3.3 Experimental Results

3.3.1 Correction of Motion Artifact

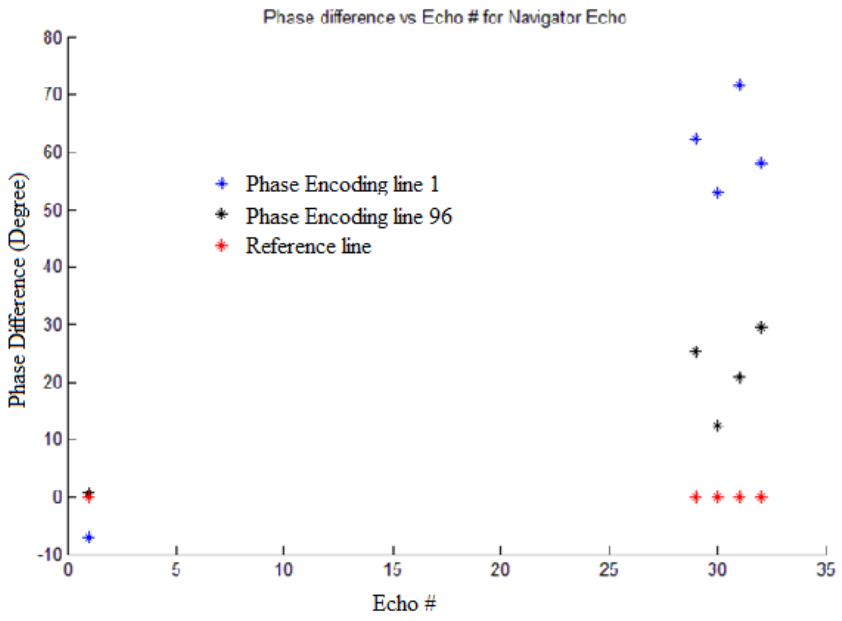

Figure 16. The phase differences between phase encoding lines (1(blue), 95(black) and reference phase encoding line 48(red), at different navigator echoes (1st and 47th-50th)

In figure 16, the relative phase differences between phase encoding lines 1 and 96 to line 48 (reference phase encoding line) were plotted as a function of the echo number (1st, 46th-50th). As shown in the figure, the phase difference varies at different echo.

For motion correction, a linear fitting was utilized to obtain the relative phase for the echoes between the first and last four navigator echoes. The derived phase difference was then applied back to the imaging echoes to correct for motion artifact.

An example of motion correction was shown as below.

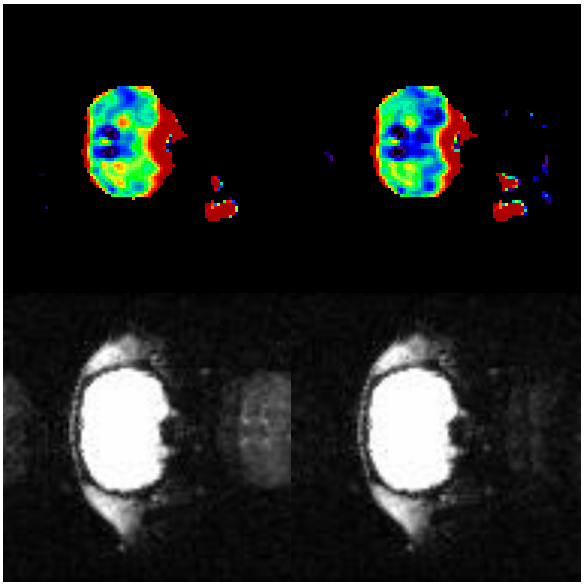

Figure 17. The R2* weighted images (bottom) and their corresponding R2' images (top) before (left) and after (right) motion correction

The R2* weighted images and their corresponding R2' images before and after motion correction were shown in figure 17. An obvious ghost was found at the edge of FOV, because the inconsistency of phase induced by the motion across phase encoding lines. With motion correction the phase inconsistency was corrected and the ghost image becomes much smaller. The derived R2' map after motion correction is smaller than that before correction. Since motion induces larger signal decay at long echo times when compared to these acquired at a shorter echo time, R2' is overestimated in the presence of motion. An effective motion corrected method will reduce R2' as shown in our results.

3.3.1.1 Optimization of GESSE Sequences

The variance of the calculated R2' depends on several factors, including the time space between echoes, the spin echo time, etc. To get optimized sequence parameters for the measurement of R2', Monte Carlo method was used to simulate the result considering the following physiology conditions, R2=24 - 27Hz, R2' = 4.061 – 20.305Hz, corresponding to OEF=0.20 – 1.00, and SNR=28 (from experimental results). The other sequence parameters are echo number =45, dTE=1.79ms, and TR=2000ms.

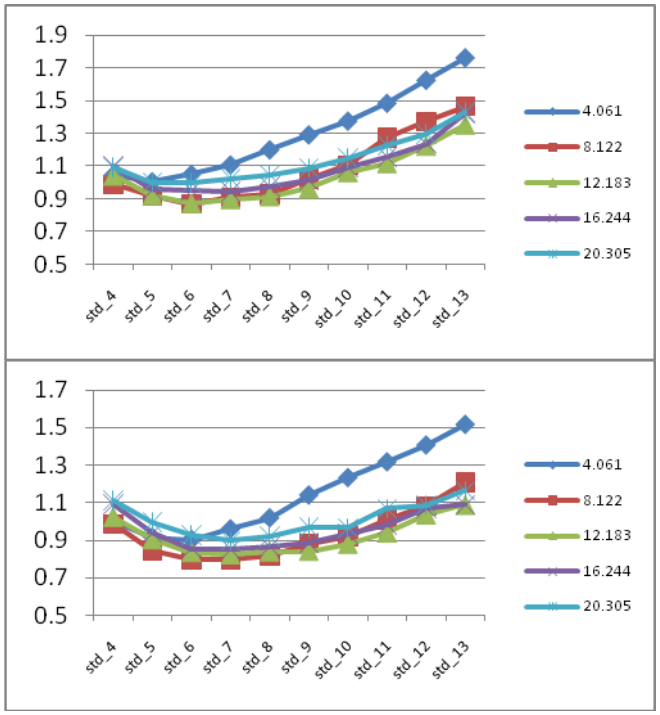

Figure 18. Upper row: R2 = 27Hz, lower row: R2 = 24Hz, x-axis is the number of echoes before the spin echo, indicating how many pairs of echoes were used for R2 estimation, y-axis is the std(Hz) of the estimation of R2'. The number in the legend is the true R2' values used for simulation, corresponding to OEF=0.20 – 1.0.

The simulation results are shown in figure 18. For R2=27Hz (24Hz), the minimal STD for R2' occurs at std_6 and std_7, with an STD of about 0.9Hz (0.75Hz). Thus, the parameter with 7 pairs of echoes before spin echo was chosen for the optimal measurement of R2'.

3.3.1.2 B0 Inhomogeneity Correction

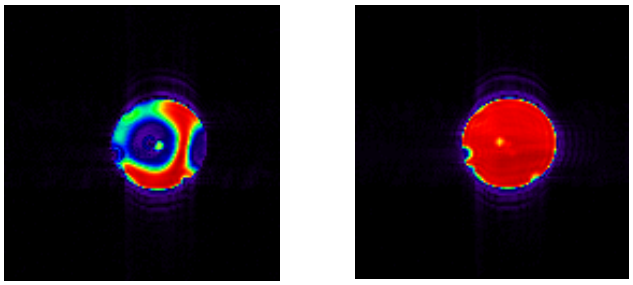

Figure 19. Phantom R2* weighted images before (left) and after (right) application of z-shimming method

For the phantom study, the high B0 inhomogeneity region produced by air bubble shifts the signal peak away from Kz=0, which leads to signal loss (low signal in the left image, figure 19). The shifted peak was sampled by additional gradients with the z shimming method and the signal was then recovered by the application of FFT along z dimension (right image, figure 19.

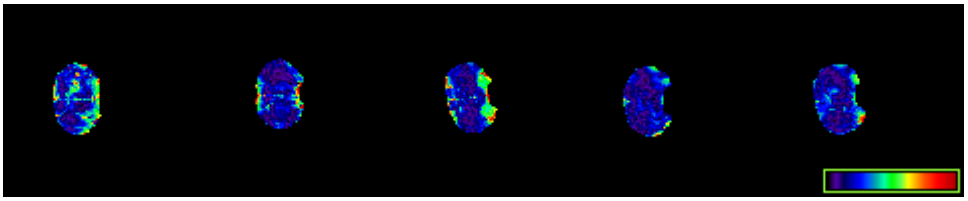

Figure 20.The dB map from 5 normal rats after careful field map shimming using a 9.4T Bruker Scanner. The scale of colorbar is 0.0ppm – 0.1ppm within 1mm thickness.

To determine the magnitude of z shimming gradients, an estimation of the magnitude of dB is necessary. As shown in figure 20, dB maps from 5 normal rats were acquired with a double echo/gradient echo sequence. With the field map shimming method on the Bruker system, a pretty uniform B0 field was obtained in most regions of brain. The B0 inhomogeneity is higher at the edge of brain, with dB value around 0.05 ppm. The magnitude of compensation gradient and the steps of gradient table are derived based on equation (3.16) and (3.17).

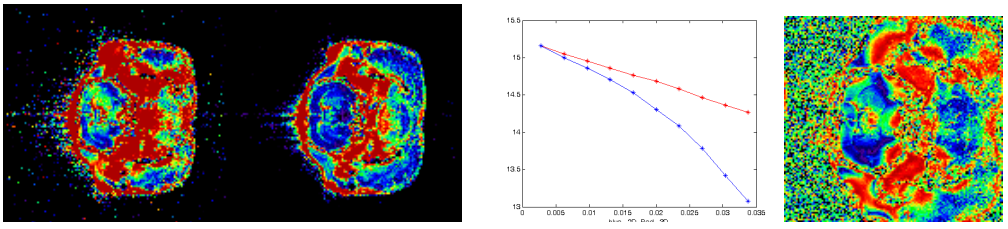

Figure 21. From left to right are the R2* weighted images before, after application of z-shimming method, typical behavior of one voxel within high B0 inhomogeneity region(before (blue) and after (red) application of z-shimming method) and the corresponding dB map.

To realize the z-shimming method, a gradient table was applied along the z direction on a multiple gradient echo sequence. Two normal animals were scanned and the R2* map was derived. As shown in figure 21, the high R2* region before applying z shimming corresponds to the high dB region. The blue curve is the signal curve as a function of time in the high B0 inhomogeneity region. Since the R2* value was derived by a linear fitting of the logarithm of signal curve (blue), the fast decay results in a high R2* value. After the application of z-shimming method, as shown by the red curve, a much smaller decay was found, which gives a more accurate estimation of the R2* value.

3.3.1.3 Consistency Test

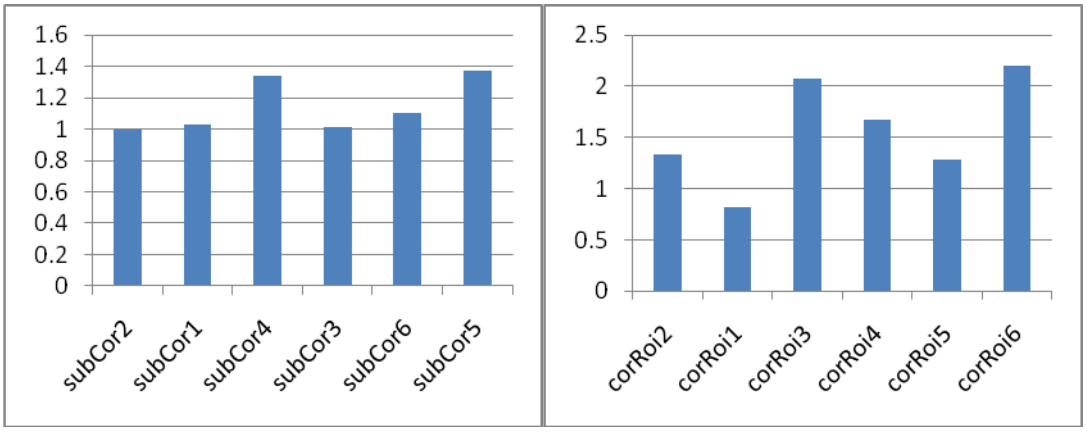

Figure 22. The STD values of mean of each ROI in subcortical (left) and cortical (right) regions

To test the consistency of our method to measure R2', 6 normal rats were scanned, with 12 ROIs defined in the cortical and subcortical regions. As shown in figure 22, the mean value of R2' is about 5 – 8 Hz in the subcortical region, while is 4 – 8 Hz in the cortical region.

In the subcortical area, the STD of R2' is less than 1.4Hz, while in the cortical area, the STD of R2' is a little bigger, with a value below 2.1Hz.

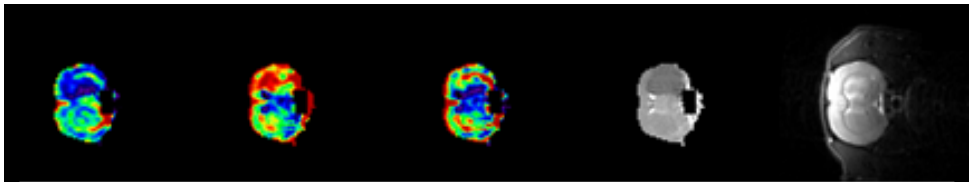

Figure 23. Typical MR images before reperfusion

The stroke study was performed using a 45 minute MCAO model. As shown in figure 23, a representative data set from an animal subjected to transient MCAO was shown. From left to right are CBF, R2’, OMI_R2’, ADC maps right before reperfusion and the corresponding registered T2w image at 24 hours after occlusion. After stroke, reduction of CBF was found at the occlusion side of the brain, while an increase of R2’ was found in the same region, with a decrease of ADC at the same time.

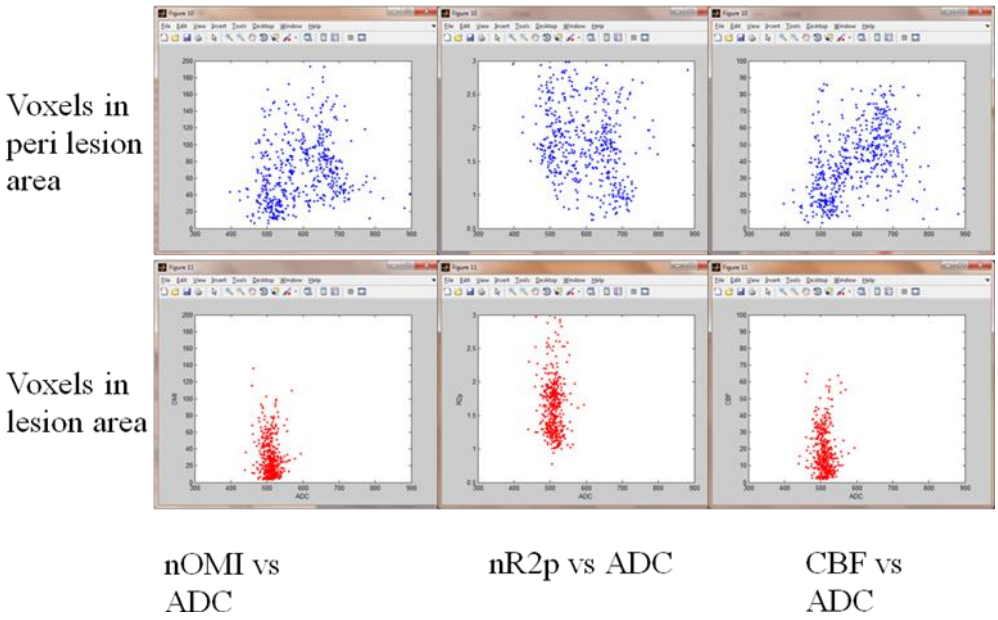

Figure 24. Red: the lesion; Blue: the region outside lesion within the same hemisphere. a) nOMI vs. ADC; b) nR2p vs. ADC; c) CBF vs. ADC.

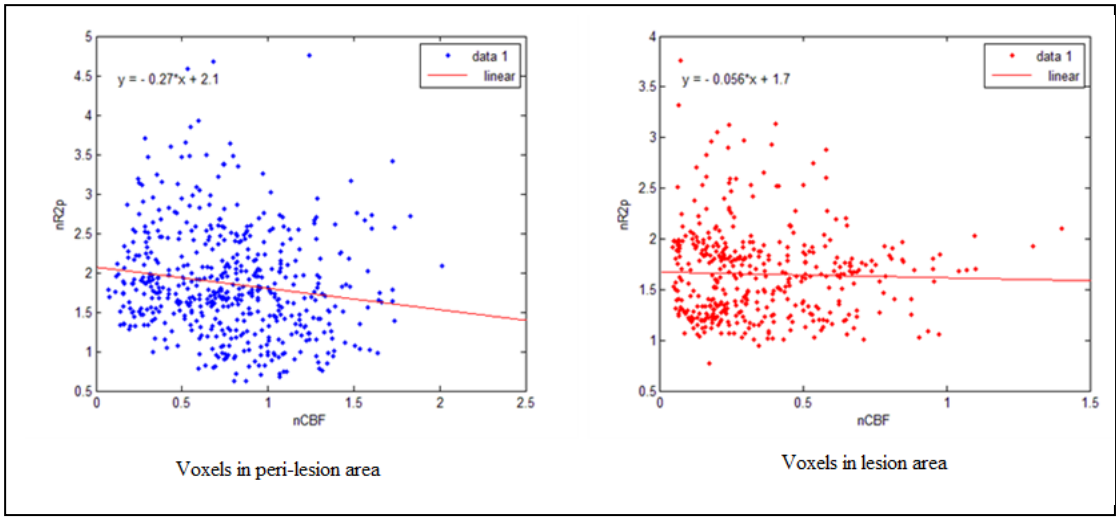

Figure 25. nR2p vs. CBF. Red: the lesion; Blue: the region outside lesion within the same hemisphere

The fates of ischemia tissue in the nOMI-ADC, nR2'-ADC and CBF-ADC were analyzed on a pixel-by-pixel basis. Figure 24 shows the scatter-plot of all the pixels from all animals in the ipsi-hemisphere. The hemisphere was subdivided into 2 groups based on the final T2w images, dead region and live region. In the CBF-ADC scatter plots, using threshold CBF=40ml/100g/min and ADC=800e-5mm2/s, the pixels in alive region can be further divided into 4 groups, with high CBF and high ADC(HH), high CBF and low ADC(HL), low CBF and high ADC (LH) and low CBF and low ADC(LL). Most pixels are in the HH and LL regions, while some pixels are in the other two regions. For the infarct region, all the voxels are within the LL region.

Figure 25 shows the scatter plots of nR2'-CBF from all animals. For the voxels in peri-lesion region, a negative pattern between R2' and CBF was observed, which indicates the increase of oxygenation with the reduction of CBF for the viable tissue. For the voxels in lesion region, there is no such pattern.

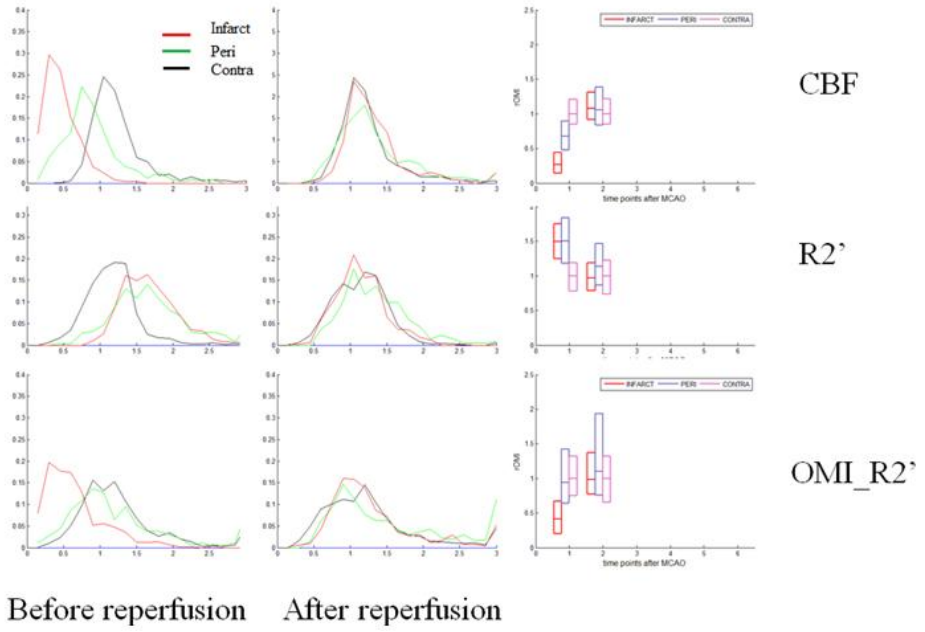

Figure 26. The histogram of CBF, R2' and OMI_R2' before and after reperfusion. The 25th, 50th and 75th percentile maps are shown in the third column.

For stroke rats, three ROIs were defined, including lesion, peri and contra. The histograms of CBF, R2' and ADC for voxels in these three regions are shown in figure 26. For CBF, the values are clearly separated between three ROIs , with the smallest CBF in lesion region, while larger in peri region and largest in contra region. The R2' is high in both the lesion region and peri region with a similar value (1.3Hz -1.7Hz) compared to the contra region (0.8Hz-1.3Hz). For the OMI_R2', the value in the peri region is similar to contra region, while much lower in the lesion region. After reperfusion, the CBF, R2' and OMI_R2' all return back to the same level as the contra region.

3.4 Conclusion and Discussion

The navigator echoes method was used for correction of motion artifacts. In our study, oral intubation was used to control the breath of animals. Teeth bar and ear bar were used to fix the head of animal, thus suppressing the motion. In most cases, the motion artifacts can be suppressed well.

There are several methods to correct for the B0 inhomogeneity. As shown in table 2, five different methods are listed. Each method has its own shortcomings. The z-shimming has a lower SNR, although it does not need the prior knowledge of the B0 inhomogeneity field or careful design of RF pulse.

The consistency of R2' is good in the subcortical region (STD<1.4Hz), while is larger (STD<2.1Hz) in the cortical region. The possible reason for the high variance of R2' in cortical region is because the cortical region is at the edge of brain, where there is a relatively higher dB effect. Although Z-shimming method was utilized to correct for the B0 inhomogeneity, it is possible that in certain animals, the dB effect is too big to be compensated for the applied gradients. Thus, the variance across animal was larger due to the different compensation effect on difference animals.

There are other ways to measure R2', such as the acquisition of R2 with a multi spin echo sequence and R2* with a gradient echo sequence separately, then the subtraction of the two is used to derive the R2'. The disadvantages of this method include the relatively long acquisition time of two sequences, making the temporal resolution low, which did not fulfill the dynamic requirement in acute stage of ischemic stroke. In addition, the diffusion effect is different in R2 and R2* sequences, which induces biases and makes the R2' overestimated. Geisler et al examined R2′ in the regions with apparent diffusion coefficient (ADC) lesion, lesion growth (recruited in the final lesion but without acute ADC abnormality) and surviving tissue . They observed an elevated R2′ in the ischemic hemisphere when compared to the unaffected hemisphere. Moreover, the ADC lesion exhibited the highest R2′, followed by the lesion growth and surviving tissue regions. Their observation suggested that an increase of R2′ may correspond to an increase of OEF in ischemia. In our study, the increase of R2' was also observed in both the infarct region and the peri-infarct region, but there is no significant difference between these two regions. The possible reason is that the subjects in our study are rats, which might have different physiology responses to ischemic stroke compared to human.

For example, in our study, the final lesion is smaller than the ADC lesion in rats, while it is usually larger than the ADC lesion as shown in Geisler's study in human.

From the histograms, the CBF can be used to separate the lesion, peri and contra regions well. Interestingly, although the OMI_R2' doesn't show better separation between lesion and peri regions compared to CBF, there is no significant difference between peri and contra region. The possible reason is, that the high R2' value in the peri region indicates an increase of oxygen extraction, thus the increase concentration of deoxy-Hb. Since OMI_R2' is the product of CBF and R2', the high R2' compensates the reduction of CBF, thus makes the OMI_R2' similar to the contra region, indicating the maintained normal metabolism of tissues in peri-lesion region. Nevertheless, for the dead region, the high R2' is unexpected. A generally held view is that dead tissue does not consume oxygen and R2' should be low instead of high in these regions. The concentration of deoxy-Hb is determined mainly by two factors: the product of deoxy-Hb, and the transportation of deoxy-Hb out of the tissue. Immediately after stroke onset, oxygen extraction fraction will increase to maintain neuronal function, resulting in an increase of deoxy-Hb. In same region with a severe reduction of CBF, the generated deoxy-Hb might not be removed effectively, which causes an accumulation of deoxy-Hb and thus the increase of R2'. Another plausible reason is that cells were still alive at the moment of imaging, but died later after reperfusion due to delayed neuronal death. Further studies are needed to fully understand this phenomenon.

CHAPTER 4

FUTURE WORK

We have developed a local brain temperature manipulation system and the MRI methods to measure the brain temperature. Moreover, we studied the changes of physiology parameters using 45 minutes MCAO under a normal body temperature condition. Future work includes further verification and analysis of these data which may shed light on the underlying mechanisms behind these changes. In addition, we will use different durations of MCAO to study whether the findings depend on elapsed times after stroke. Finally, we will study how hypothermia may alter the course of ischemic progression using these physiological parameters.

REFERENCES

1. Williams, D.S., et al., *Magnetic resonance imaging of perfusion using spin inversion of arterial water.* Proc Natl Acad Sci U S A, 1992. **89**(1): p. 212-6.

2. *Tissue plasminogen activator for acute ischemic stroke. The National Institute of Neurological Disorders and Stroke rt-PA Stroke Study Group.* N Engl J Med, 1995. **333**(24): p. 1581-7.

3. Fisher, M., M.S. Pessin, and A.J. Furian, *ECASS: lessons for future thrombolytic stroke trials. European Cooperative Acute Stroke Study.* Jama, 1995. **274**(13): p. 1058-9.

4. Hacke, W., et al., *Randomised double-blind placebo-controlled trial of thrombolytic therapy with intravenous alteplase in acute ischaemic stroke (ECASS II). Second European-Australasian Acute Stroke Study Investigators.* Lancet, 1998. **352**(9136): p. 1245-51.

5. Levi, C.R., *Tissue plasminogen activator (tPA) in acute ischaemic stroke: time for collegiate communication and consensus.* Med J Aust, 2004. **180**(12): p. 634-6.

6. Laloux, P., *Intravenous rtPA thrombolysis in acute ischemic stroke.* Acta Neurol Belg, 2001. **101**(2): p. 88-95.

7. Hacke, W., et al., *Thrombolysis with alteplase 3 to 4.5 hours after acute ischemic stroke.* N Engl J Med, 2008. **359**(13): p. 1317-29.

8. Kidwell, C.S., J.R. Alger, and J.L. Saver, *Beyond mismatch: evolving paradigms in imaging the ischemic penumbra with multimodal magnetic resonance imaging.* Stroke, 2003. **34**(11): p. 2729-35.

9. Li, F., et al., *Transient and permanent resolution of ischemic lesions on diffusion-weighted imaging after brief periods of focal ischemia in rats : correlation with histopathology.* Stroke, 2000. **31**(4): p. 946-54.

10. Li, F., et al., *Secondary decline in apparent diffusion coefficient and neurological outcomes after a short period of focal brain ischemia in rats.* Annals of Neurology, 2000. **48**(2): p. 236-44.

11. Li, F., et al., *Temporal evolution of ischemic injury evaluated with diffusion-, perfusion-, and T2-weighted MRI.* Neurology, 2000. **54**(3): p. 689-96.

12. Kidwell, C.S., et al., *Diffusion MRI in patients with transient ischemic attacks. [see comments]*. Stroke, 1999. **30**(6): p. 1174-80.

13. Kidwell, C.S., et al., *Thrombolytic reversal of acute human cerebral ischemic injury shown by diffusion/perfusion magnetic resonance imaging.* Annals of Neurology, 2000. **47**(4): p. 462-9.

14. Powers, W.J., et al., *Cerebral blood flow and cerebral metabolic rate of oxygen requirements for cerebral function and viability in humans.* J Cereb Blood Flow Metab, 1985. **5**(4): p. 600-8.

15. Frykholm, P., et al., *A metabolic threshold of irreversible ischemia demonstrated by PET in a middle cerebral artery occlusion-reperfusion primate model.* Acta Neurol Scand, 2000. **102**(1): p. 18-26.

16. Young, A.R., et al., *Relationships between high oxygen extraction fraction in the acute stage and final infarction in reversible middle cerebral artery occlusion: an investigation in anesthetized baboons with positron emission tomography.* J Cereb Blood Flow Metab, 1996. **16**(6): p. 1176-88.

17. Giffard, C., et al., *Outcome of acutely ischemic brain tissue in prolonged middle cerebral artery occlusion: a serial positron emission tomography investigation in the baboon.* J Cereb Blood Flow Metab, 2004. **24**(5): p. 495-508.

18. Busto, R., et al., *Effect of mild hypothermia on ischemia-induced release of neurotransmitters and free fatty acids in rat brain.* Stroke, 1989. **20**(7): p. 904-10.

19. Huh, P.W., et al., *Comparative neuroprotective efficacy of prolonged moderate intraischemic and postischemic hypothermia in focal cerebral ischemia.* J Neurosurg, 2000. **92**(1): p. 91-9.

20. Reith, J., et al., *Body temperature in acute stroke: relation to stroke severity, infarct size, mortality, and outcome.* Lancet, 1996. **347**(8999): p. 422-5.

21. Ginsberg, M.D. and W.A. Pulsinelli, *The ischemic penumbra, injury thresholds, and the therapeutic window for acute stroke.* Ann Neurol, 1994. **36**(4): p. 553-4.

22. Astrup, J., B.K. Siesjo, and L. Symon, *Thresholds in cerebral ischemia - the ischemic penumbra.* Stroke, 1981. **12**(6): p. 723-5.

23. Astrup, J., et al., *Cortical evoked potential and extracellular K+ and H+ at critical levels of brain ischemia.* Stroke, 1977. **8**(1): p. 51-7.

24. Siesjo, B.K., *Pathophysiology and treatment of focal cerebral ischemia. Part I: Pathophysiology.* J Neurosurg, 1992. **77**(2): p. 169-84.

25. Hossmann, K.A., *Viability thresholds and the penumbra of focal ischemia.* Ann Neurol, 1994. **36**(4): p. 557-65.

26. Heiss, W.D., et al., *Dynamic penumbra demonstrated by sequential multitracer PET after middle cerebral artery occlusion in cats.* J Cereb Blood Flow Metab, 1994. **14**(6): p. 892-902.

27. Heiss, W.D., et al., *Progressive derangement of periinfarct viable tissue in ischemic stroke.* J Cereb Blood Flow Metab, 1992. **12**(2): p. 193-203.

28. Heiss, W.D. and R. Graf, *The ischemic penumbra.* Curr Opin Neurol, 1994. **7**(1): p. 11-9.

29. Pappata, S., et al., *PET study of changes in local brain hemodynamics and oxygen metabolism after unilateral middle cerebral artery occlusion in baboons.* J Cereb Blood Flow Metab, 1993. **13**(3): p. 416-24.

30. Furlan, A., et al., *Intra-arterial prourokinase for acute ischemic stroke. The PROACT II study: a randomized controlled trial. Prolyse in Acute Cerebral Thromboembolism.* Jama, 1999. **282**(21): p. 2003-11.

31. Marchal, G., et al., *Prolonged persistence of substantial volumes of potentially viable brain tissue after stroke: a correlative PET-CT study with voxel-based data analysis.* Stroke, 1996. **27**(4): p. 599-606.

32. Read, S.J., et al., *The fate of hypoxic tissue on 18F-fluoromisonidazole positron emission tomography after ischemic stroke.* Ann Neurol, 2000. **48**(2): p. 228-35.

33. Rother, J., et al., *Effect of intravenous thrombolysis on MRI parameters and functional outcome in acute stroke <6 hours.* Stroke, 2002. **33**(10): p. 2438-45.

34. Heiss, W.D. and J. Sobesky, *Comparison of PET and DW/PW-MRI in acute ischemic stroke.* Keio J Med, 2008. **57**(3): p. 125-31.

35. Takata, T., M. Nabetani, and Y. Okada, *Effects of hypothermia on the neuronal activity, [Ca2+]i accumulation and ATP levels during oxygen and/or glucose deprivation in hippocampal slices of guinea pigs.* Neurosci Lett, 1997. **227**(1): p. 41-4.

36. Bacher, A., J.Y. Kwon, and M.H. Zornow, *Effects of temperature on cerebral tissue oxygen tension, carbon dioxide tension, and pH during transient global ischemia in rabbits.* Anesthesiology, 1998. **88**(2): p. 403-9.

37. Lanier, W.L., *Cerebral metabolic rate and hypothermia: their relationship with ischemic neurologic injury.* J Neurosurg Anesthesiol, 1995. **7**(3): p. 216-21.

38. Sakoh, M. and A. Gjedde, *Neuroprotection in hypothermia linked to redistribution of oxygen in brain.* Am J Physiol Heart Circ Physiol, 2003. **285**(1): p. H17-25.

39. Rosomoff, H.L. and D.A. Holaday, *Cerebral blood flow and cerebral oxygen consumption during hypothermia.* Am J Physiol, 1954. **179**(1): p. 85-8.

40. Maier, C.M., et al., *Effects of mild hypothermia on superoxide anion production, superoxide dismutase expression, and activity following transient focal cerebral ischemia.* Neurobiol Dis, 2002. **11**(1): p. 28-42.

41. Kil, H.Y., J. Zhang, and C.A. Piantadosi, *Brain temperature alters hydroxyl radical production during cerebral ischemia/reperfusion in rats.* J Cereb Blood Flow Metab, 1996. **16**(1): p. 100-6.

42. Globus, M.Y., et al., *Glutamate release and free radical production following brain injury: effects of posttraumatic hypothermia.* J Neurochem, 1995. **65**(4): p. 1704-11.

43. Lei, B., N. Adachi, and T. Arai, *The effect of hypothermia on H2O2 production during ischemia and reperfusion: a microdialysis study in the gerbil hippocampus.* Neurosci Lett, 1997. **222**(2): p. 91-4.

44. Wenisch, C., et al., *Mild intraoperative hypothermia reduces production of reactive oxygen intermediates by polymorphonuclear leukocytes.* Anesth Analg, 1996. **82**(4): p. 810-6.

45. Winfree, C.J., et al., *Mild hypothermia reduces penumbral glutamate levels in the rat permanent focal cerebral ischemia model.* Neurosurgery, 1996. **38**(6): p. 1216-22.

46. Takagi, K., et al., *Effect of hyperthermia on glutamate release in ischemic penumbra after middle cerebral artery occlusion in rats.* Am J Physiol, 1994. **267**(5 Pt 2): p. H1770-6.

47. Nakashima, K. and M.M. Todd, *Effects of hypothermia on the rate of excitatory amino acid release after ischemic depolarization.* Stroke, 1996. **27**(5): p. 913-8.

48. Maier, C.M., et al., *Optimal depth and duration of mild hypothermia in a focal model of transient cerebral ischemia: effects on neurologic outcome, infarct size, apoptosis, and inflammation.* Stroke, 1998. **29**(10): p. 2171-80.

49. Xu, L., et al., *Mild hypothermia reduces apoptosis of mouse neurons in vitro early in the cascade.* J Cereb Blood Flow Metab, 2002. **22**(1): p. 21-8.

50. Yenari, M.A., et al., *Mild hypothermia attenuates cytochrome c release but does not alter Bcl-2 expression or caspase activation after experimental stroke.* J Cereb Blood Flow Metab, 2002. **22**(1): p. 29-38.

51. Karibe, H., et al., *Mild intraischemic hypothermia reduces postischemic hyperperfusion, delayed postischemic hypoperfusion, blood-brain barrier disruption, brain edema, and neuronal damage volume after temporary focal cerebral ischemia in rats.* J Cereb Blood Flow Metab, 1994. **14**(4): p. 620-7.

52. Huang, Z.G., et al., *Biphasic opening of the blood-brain barrier following transient focal ischemia: effects of hypothermia.* Can J Neurol Sci, 1999. **26**(4): p. 298-304.

53. Kawai, N., et al., *Effects of hypothermia on thrombin-induced brain edema formation.* Brain Res, 2001. **895**(1-2): p. 50-8.

54. Kollmar, R., et al., *Neuroprotective effect of delayed moderate hypothermia after focal cerebral ischemia: an MRI study.* Stroke, 2002. **33**(7): p. 1899-904.

55. Bernard, S.A., et al., *Treatment of comatose survivors of out-of-hospital cardiac arrest with induced hypothermia.* N Engl J Med, 2002. **346**(8): p. 557-63.

56. Shankaran, S., et al., *Whole-body hypothermia for neonates with hypoxic-ischemic encephalopathy.* N Engl J Med, 2005. **353**(15): p. 1574-84.

57. Castillo, J., et al., *Timing for fever-related brain damage in acute ischemic stroke.* Stroke, 1998. **29**(12): p. 2455-60.

58. van der Worp, H.B., et al., *Hypothermia in animal models of acute ischaemic stroke: a systematic review and meta-analysis.* Brain, 2007. **130**(Pt 12): p. 3063-74.

59. Schwab, S., et al., *Moderate hypothermia in the treatment of patients with severe middle cerebral artery infarction.* Stroke, 1998. **29**(12): p. 2461-6.

60. Schwab, S., et al., *Feasibility and safety of moderate hypothermia after massive hemispheric infarction.* Stroke, 2001. **32**(9): p. 2033-5.

61. Krieger, D.W., et al., *Cooling for acute ischemic brain damage (cool aid): an open pilot study of induced hypothermia in acute ischemic stroke.* Stroke, 2001. **32**(8): p. 1847-54.

62. Georgiadis, D., et al., *Endovascular cooling for moderate hypothermia in patients with acute stroke: first results of a novel approach.* Stroke, 2001. **32**(11): p. 2550-3.

63. De Georgia, M.A., et al., *Cooling for Acute Ischemic Brain Damage (COOL AID): a feasibility trial of endovascular cooling.* Neurology, 2004. **63**(2): p. 312-7.

64. Busto, R., et al., *Small differences in intraischemic brain temperature critically determine the extent of ischemic neuronal injury.* J Cereb Blood Flow Metab, 1987. **7**(6): p. 729-38.

65. Ginsberg, M.D. and R. Busto, *Combating hyperthermia in acute stroke: a significant clinical concern.* Stroke, 1998. **29**(2): p. 529-34.

66. Ginsberg, M.D., et al., *Therapeutic modulation of brain temperature: relevance to ischemic brain injury.* Cerebrovasc Brain Metab Rev, 1992. **4**(3): p. 189-225.

67. Kawai, N., et al., *Effects of delayed intraischemic and postischemic hypothermia on a focal model of transient cerebral ischemia in rats.* Stroke, 2000. **31**(8): p. 1982-9; discussion 1989.

68. Zhang, R.L., et al., *Postischemic (1 hour) hypothermia significantly reduces ischemic cell damage in rats subjected to 2 hours of middle cerebral artery occlusion.* Stroke, 1993. **24**(8): p. 1235-40.

69. Onesti, S.T., et al., *Transient hypothermia reduces focal ischemic brain injury in the rat.* Neurosurgery, 1991. **29**(3): p. 369-73.

70. Baker, C.J., et al., *Hypothermic protection following middle cerebral artery occlusion in the rat.* Surg Neurol, 1991. **36**(3): p. 175-80.

71. Kader, A., et al., *The effect of mild hypothermia on permanent focal ischemia in the rat.* Neurosurgery, 1992. **31**(6): p. 1056-60; discussion 1060-1.

72. Baker, C.J., S.T. Onesti, and R.A. Solomon, *Reduction by delayed hypothermia of cerebral infarction following middle cerebral artery occlusion in the rat: a time-course study.* J Neurosurg, 1992. **77**(3): p. 438-44.

73. Markarian, G.Z., et al., *Mild hypothermia: therapeutic window after experimental cerebral ischemia.* Neurosurgery, 1996. **38**(3): p. 542-50; discussion 551.

74. Colbourne, F., et al., *Prolonged but delayed postischemic hypothermia: a long-term outcome study in the rat middle cerebral artery occlusion model.* J Cereb Blood Flow Metab, 2000. **20**(12): p. 1702-8.

75. Corbett, D., M. Hamilton, and F. Colbourne, *Persistent neuroprotection with prolonged postischemic hypothermia in adult rats subjected to transient middle cerebral artery occlusion.* Exp Neurol, 2000. **163**(1): p. 200-6.

76. Maier, C.M., et al., *Delayed induction and long-term effects of mild hypothermia in a focal model of transient cerebral ischemia: neurological outcome and infarct size.* J Neurosurg, 2001. **94**(1): p. 90-6.

77. Du, C., et al., *Very delayed infarction after mild focal cerebral ischemia: a role for apoptosis?* J Cereb Blood Flow Metab, 1996. **16**(2): p. 195-201.

78. Brix, G., et al., *Fast and precise T1 imaging using a TOMROP sequence.* Magn Reson Imaging, 1990. **8**(4): p. 351-6.

79. Parker, D.L., et al., *Temperature distribution measurements in two-dimensional NMR imaging.* Med Phys, 1983. **10**(3): p. 321-5.

80. Dickinson, R.J., et al., *Measurement of changes in tissue temperature using MR imaging.* J Comput Assist Tomogr, 1986. **10**(3): p. 468-72.

81. Quesson, B., J.A. de Zwart, and C.T. Moonen, *Magnetic resonance temperature imaging for guidance of thermotherapy.* J Magn Reson Imaging, 2000. **12**(4): p. 525-33.

82. Calamante, F., et al., *Measuring cerebral blood flow using magnetic resonance imaging techniques.* J Cereb Blood Flow Metab, 1999. **19**(7): p. 701-35.

83. Longa, E.Z., et al., *Reversible middle cerebral artery occlusion without craniectomy in rats.* Stroke, 1989. **20**(1): p. 84-91.

84. Laptook, A.R., L. Shalak, and R.J. Corbett, *Differences in brain temperature and cerebral blood flow during selective head versus whole-body cooling.* Pediatrics, 2001. **108**(5): p. 1103-10.

85. Ewing, J.R., et al., *T1 and magnetization transfer at 7 Tesla in acute ischemic infarct in the rat.* Magn Reson Med, 1999. **41**(4): p. 696-705.

86. Kettunen, M.I., et al., *Interrelations of T(1) and diffusion of water in acute cerebral ischemia of the rat.* Magn Reson Med, 2000. **44**(6): p. 833-9.

87. Calamante, F., et al., *Early changes in water diffusion, perfusion, T1, and T2 during focal cerebral ischemia in the rat studied at 8.5 T.* Magn Reson Med, 1999. **41**(3): p. 479-85.

88. Lythgoe, M.F., et al., *Acute changes in MRI diffusion, perfusion, T(1), and T(2) in a rat model of oligemia produced by partial occlusion of the middle cerebral artery.* Magn Reson Med, 2000. **44**(5): p. 706-12.

89. Alsop, D.C. and J.A. Detre, *Reduced transit-time sensitivity in noninvasive magnetic resonance imaging of human cerebral blood flow.* J Cereb Blood Flow Metab, 1996. **16**(6): p. 1236-49.

90. Grohn, O.H.J., et al., *Early detection of irreversible cerebral ischemia in the rat using dispersion of the magnetic resonance imaging relaxation time, T1rho.* J Cereb Blood Flow Metab, 2000. **20**(10): p. 1457-66.

91. Rosen, B.R., J.W. Belliveau, and D. Chien, *Perfusion imaging by nuclear magnetic resonance.* Magn Reson Q, 1989. **5**(4): p. 263-81.

92. Wu, O., et al., *Tracer arrival timing-insensitive technique for estimating flow in MR perfusion-weighted imaging using singular value decomposition with a block-circulant deconvolution matrix.* Magn Reson Med, 2003. **50**(1): p. 164-74.

93. Yablonskiy, D.A. and E.M. Haacke, *Theory of NMR signal behavior in magnetically inhomogeneous tissues: the static dephasing regime.* Magn Reson Med, 1994. **32**(6): p. 749-63.

94. An, H. and W. Lin, *Cerebral oxygen extraction fraction and cerebral venous blood volume measurements using MRI: effects of magnetic field variation.* Magn Reson Med, 2002. **47**(5): p. 958-66.

95. Ordidge, R.J., et al., *Correction of motional artifacts in diffusion-weighted MR images using navigator echoes.* Magn Reson Imaging, 1994. **12**(3): p. 455-60.

96. McGee, K.P., et al., *Rapid autocorrection using prescan navigator echoes.* Magn Reson Med, 2000. **43**(4): p. 583-8.

97. Anderson, A.W. and J.C. Gore, *Analysis and correction of motion artifacts in diffusion weighted imaging.* Magn Reson Med, 1994. **32**(3): p. 379-87.

98. Jezzard, P. and R.S. Balaban, *Correction for geometric distortion in echo planar images from B0 field variations.* Magn Reson Med, 1995. **34**(1): p. 65-73.

99. Yang, Q.X., et al., *Removal of local field gradient artifacts in T2*-weighted images at high fields by gradient-echo slice excitation profile imaging.* Magn Reson Med, 1998. **39**(3): p. 402-9.

100. Wardlaw, J.M., *Neuroimaging in acute ischaemic stroke: insights into unanswered questions of pathophysiology.* J Intern Med. **267**(2): p. 172-90.